New insights into the eastern Subpolar North Atlantic meridional overturning circulation from OVIDE

Herlé Mercier[1], Damien Desbruyères[1], Pascale Lherminier[1], Antón Velo[2], Lidia Carracedo[1], Marcos Fontela[2,3], Fiz F. Pérez[2]

[1]University of Brest, CNRS, Ifremer, IRD, Laboratoire d'Océanographie Physique et Spatiale (LOPS), IUEM, Plouzané, 29280, France

[2]Instituto de Investigaciones Marinas (IIM), CSIC, Vigo, 36208, Spain

[3]Center of Marine Sciences (CCMAR), Universidade do Algarve, 8005-139 Faro, Portugal

Correspondence to: Herlé Mercier (Herle.Mercier@ifremer.fr)

Abstract. The Atlantic Meridional Overturning Circulation (AMOC) is a key component of the Earth's climate. However, there are few long series of observations of the AMOC and the study of the mechanisms driving its variability depends mainly on numerical simulations. Here, we use four ocean circulation estimates produced by different data-driven approaches of increasing complexity to analyze the seasonal to decadal variability of the subpolar AMOC across the Greenland–Portugal OVIDE line since 1993. We decompose the MOC strength variability into a velocity-driven component due to circulation changes and a volume-driven component due to changes in the depth of the overturning maximum isopycnal. We show that the variance of the time series is dominated by seasonal variability, which is due to both seasonal variability in the volume of the AMOC limbs (linked to the seasonal cycle of density in the East Greenland Current) and to seasonal variability in the transport of the Eastern Boundary Current. The decadal variability of the subpolar AMOC is mainly caused by changes in velocity, which after the mid-2000s are partly offset by changes in the volume of the AMOC limbs. This compensation means that the decadal variability of the AMOC is weaker and therefore more difficult to detect than the decadal variability of its velocity-driven and volume-driven components, which is highlighted by the formalism that we propose.

Short summary for the general audience. Here, we study the Atlantic Meridional Overturning Circulation (AMOC) measured between Greenland and Portugal between 1993–2021. We identify changes in AMOC limb volume and velocity as two major drivers of AMOC variability at subpolar latitudes. Volume variations dominate on the seasonal time scale, while velocity variations are more important on the decadal time scale. This decomposition proves useful for understanding the origin of the differences between AMOC time series from different analyses.

1 Introduction

The Atlantic Meridional Overturning Circulation (AMOC) is key in the climate system through the uptake and redistribution of heat, freshwater, and dissolved inorganic carbon across latitudes in the Atlantic Ocean (e. g. Pérez et al. 2013; Bryden et. al., 2020; Williams et al., 2021; Messias and Mercier, 2022). Paleoclimatic evidence suggests that abrupt changes in North Atlantic climate occurred during glacial and interglacial periods, with transition periods of a few decades, and identifies AMOC as a key feature associated with these abrupt changes (Lynch-Stieglitz, 2007). Today, as the climate is perturbed by human activity, climate projections suggest that the AMOC will decrease in response to anthropogenic forcing (Weijer et al., 2020). However, the magnitude and timing of this decline remains uncertain and it is still not known whether this decline has already begun. This critical role of the AMOC in climate change has highlighted the need to monitor its evolution under current anthropogenic forcing and has prompted unprecedented efforts over the past decades to establish AMOC observing systems (Srokosz and Bryden, 2015; Frajka-Williams et al., 2019; McCarthy et al., 2019).

In the subtropical North Atlantic, the trans-Atlantic RAPID network (26.5°N), deployed since 2004, has shown variability in the MOC from weeks to decades (Srokosz and Bryden, 2015; we use the acronym MOC to designate a measure of the AMOC at a specific location), consistent with that of the Meridional Overturning Variability Experiment (MOVE) network at 16°N (Jackson et al., 2022). A notable feature in this time series is that the MOC has shifted to a reduced circulation state since 2008 (Smeed et al., 2018) with hints of a potential recovery in recent years (Moat et al, 2020). A second signal of interest is a wind-forced sharp decrease in the amplitude of the MOC for several months in 2009 that created a heat transport anomaly partly responsible for the decrease in the heat content of the subpolar gyre half a decade later (Bryden et al., 2020). Using a proxy method which makes it possible to study a longer period, Worthington et al. (2021) concluded that there has been no decline in MOC at 26.5°N since the early 1980s. At seasonal to interannual time scales, MOC variability at 26.5°N has been shown to be related to the variability in the wind stress curl through variability of the Ekman transport and mediation by Rossby waves (Zhao and Johns 2014a, b; Kansow et al. 2010).

In the subpolar latitudes of the North Atlantic, the Overturning in the Subpolar North Atlantic Program (OSNAP) network, which covers the Labrador Sea, the Irminger Sea and the Iceland Basin to the Scottish Shelf, operates since 2014. OSNAP has also revealed significant variability for all resolved frequencies (Li et al., 2021). The MOC time series at OVIDE (Observatoire de la Variabilité Interannuelle à DÉcennale), which used hydrography and altimetry to reconstruct the MOC between Greenland and Portugal since 1993 (Mercier et al., 2015; Frakja-Williams, 2019; Figure 1 for section location), also shows strong variability at all resolved time scales. OSNAP has highlighted the dominant role of the eastern subpolar gyre in shaping the mean state and the variability of the MOC, with most of the subpolar overturning occurring between Greenland and Scotland (Lozier et al. 2019; Li et al., 2021). The low-frequency variability of the MOC in the subpolar gyre has been linked to the variability of buoyancy fluxes to the north of the observation sections on multi-year time scales (Desbruyères et al., 2019), with storage becoming important on shorter time scales (Petit et al., 2020). At intra-annual frequencies, MOC seasonality at OSNAP can be explained by both the seasonality in the water mass transformation and the seasonality in the Ekman transport (Fu et al., 2023). Considering OSNAP-East (Figure 1), Wang et al. (2021) established a link between MOC seasonality and seasonal displacement in the Irminger Basin of σ_{moc}, the isopycnal separating the MOC upper limb from the lower limb. Tooth et al. (2023) concluded that seasonality in the upper East Greenland Current (EGC) transport must also be considered to explain the full seasonality of the MOC across OSNAP-East. A remarkable feature of the North Atlantic subpolar gyre is its deep convection sites in the Labrador Sea, southeast Greenland and Irminger Sea, subject to significant interannual to decadal variations in the properties (e.g. density) and volumes of the water masses formed (Yashayaev and Loder, 2016; Piron et al., 2016; de Jong et al., 2018; Zunino et al.

2020). This variability in the density of the 0–1000 m layer in the Irminger Sea has been shown to be a key player in setting the MOC strength on interannual to decadal timescales (Chafik et al., 2022).

75
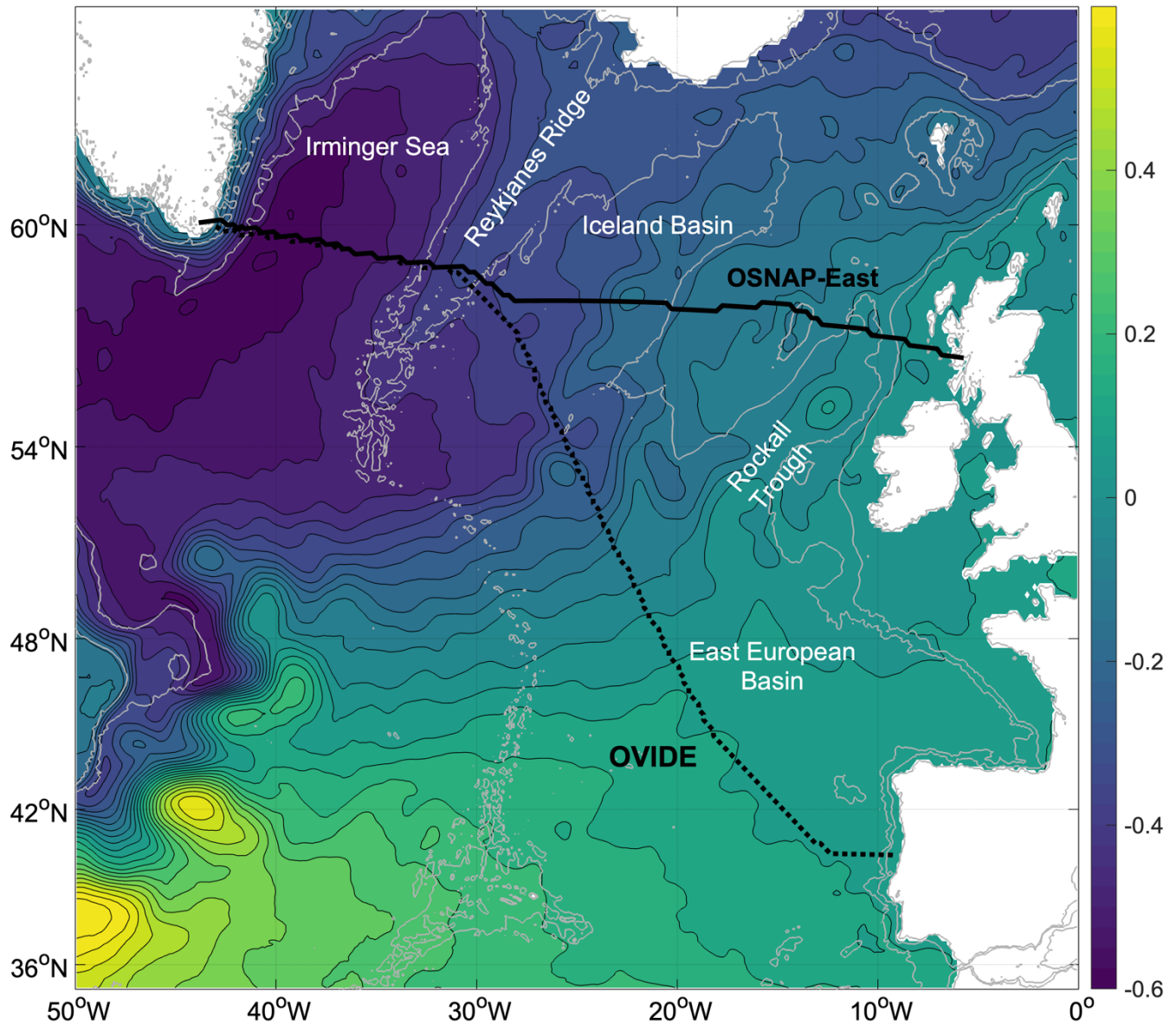
Figure 1: OVIDE and OSNAP-East lines plotted over the mean over 1993–2012 of the AVISO surface dynamic topography (cm) (Jousset et al., 2022). The 200 and 2000 meters isobaths are plotted in grey.

80 The relationship between subpolar and subtropical latitude AMOC is the subject of a large number of studies. Among them, some have linked density variations in the central Labrador Sea to the strength of the AMOC at subtropical latitudes (e.g. Böning et al., 2006; Robson et al., 2014; Yeager et al., 2021). These density anomalies are thought to spread southwards from the Labrador Sea along the deep western boundary current or by interior routes (e.g. Zhang et al., 2010), thus modifying the zonal density gradient and consequently the AMOC. Intriguingly, observations at 26.5°N show that most of the variability observed

85 in the deep western boundary current does not occur at the level of the Labrador Sea Water (LSW) but below it in the Lower North Atlantic Deep Water (LNADW), a water mass originating from the Nordic Seas (McCarthy et al., 2012; Smeed et al., 2014; Zou et al., 2018; Johns et al., 2023). In a recent numerical study, Kostov et al. (2023) proposed mechanisms, activated by density anomalies at the south-western boundary of the Labrador Sea, by which the North Atlantic Current (NAC), and thus the eastern subpolar gyre, plays a central role in linking Labrador Sea surface density anomalies to LNADW variability at RAPID

90 in about half a decade. On decadal time scales, Desbruyères et al. (2013) showed that the decadal variability of the MOC across

the OVIDE line is associated with synchronized changes in the NAC subpolar and subtropical components, the latter being the main source of variability and providing a link between subtropical and subpolar variability. Nevertheless, the fact that the drivers of AMOC variability depend on the latitude at which the AMOC is studied (e.g. Kostov et al., 2021) complicates the identification in the observations of a connection between the subpolar AMOC and the subtropical AMOC. To achieve this latter goal, sustained networks of observations to better understand the variability of the AMOC and its components as well as synergies with modeling and theoretical studies must be pursued. Here, we study the variability of the eastern subpolar AMOC and its link with the variability of its components.

The aim of this article is to analyse MOC strength time series across the OVIDE line between 1993 and 2021 in terms of seasonal to decadal variability. This work is based on four time series whose common feature is that they were derived using data-driven approaches of varying complexity, which complements recent studies based on prognostic numerical simulations. We show that the variability of the MOC at OVIDE can be effectively decomposed into a volume-driven term, linked to changes in the volume of the MOC branches at constant velocity, and a velocity-driven term at constant volume, which sheds light on the mechanisms of the observed seasonal to decadal variability. The data are presented in section 2, the methodology in section 3, the results in section 4. We end the paper with a discussion in section 5 and concluding remarks in section 6.

2 Data

2.1 OVIDE hydrographic data

We used the Greenland to Portugal OVIDE hydrographic line, referred to as A25 by GO-SHIP (Global Ocean Ship-based Hydrographic Investigations Program, Sloyan et al., 2019), which was occupied every second year between 2002 and 2018 and repeated again in 2021 (Figure 1). The surveys last about three weeks and have always been carried out between May and July. The FOUREX hydrographic line carried out in August–September 1997 along a nearby track was also used. Each section comprises at least 92 hydrographic stations with a nominal station spacing of 25 NM reduced to 10 NM or less over continental slopes and oceanic ridges with the exception of the 2014 occupation that, due to limited ship-time and repeated stations for sampling GEOTRACES program core parameters, had coarser station spacing away from fronts and boundary currents (Lherminier et al., 2007; Lherminier et al., 2010; Gourcuff et al., 2011; Mercier et al., 2015; Zunino et al., 2017). FOUREX and OVIDE temperature, pressure, and conductivity measurement accuracies meet the GO-SHIP requirements (Sloyan et al., 2019).

2.2 Objective analyses of temperature and salinity measurements

Coriolis Ocean dataset for ReAnalysis (CORA) is a global objective analysis of delayed-mode quality controlled in situ temperature and salinity profiles (Szekely et al., 2019). Here, we used CORA v5.2 monthly gridded fields from 1993 to 2021. CORA v5.2 grid horizontal resolution is 0.5° x cosine(latitude) in latitude and 0.5° in longitude, and it has 152 irregularly spaced depth levels. Maximum analysis depth is 2000 m.

EN4 is a collection of objective analyses of potential temperature and salinity profiles (Good et al., 2013). Here, we used EN4 version 4.2.2 monthly gridded fields with the bias corrections from Cheng et al. (2014) for the time period from 1993 through 2021. EN4 provides gridded fields of potential temperature and salinity with associated errors, with a monthly temporal resolution, 1° by 1° horizontal resolution and 42 irregularly spaced depth levels.

We defined a grid along the path of the OVIDE line, referred herein as the OVIDE line grid, with a horizontal resolution of 7 km and vertical resolution of 1 m. The CORA v5.2 and EN4 temperature and salinity fields were linearly interpolated to the locations of the OVIDE line grid.

2.3 GloSea5 reanalysis

GloSea5 is an ocean reanalysis based on the ensemble prediction system built around the high-resolution version of the Met Office climate prediction model: HadGEM3 family atmosphere-ocean coupled climate model (MacLachlan et al., 2015; Scaife et al., 2014). The reanalysis uses most of available satellite and in situ data and an incremental three-dimensional variational first guess at appropriate time (FGAT) data assimilation system (Jackson et al., 2016; MacLachlan et al., 2015). Increments are applied to temperature and salinity fields. The ocean general circulation model is the Nucleus for European Modelling of the Ocean (NEMO) model in its ORCA0.25 configuration (0.25° horizontal resolution with 75 irregularly spaced vertical levels). GloSea5 reanalysis is distributed by Copernicus Marine Environment Monitoring Service (CMEMS) in interpolated form on a grid common to other reanalyses. For better accuracy of transport determination, here we used the monthly fields of potential temperature, salinity and velocity from GloSea5 on the ORCA025 native grid along the OVIDE line, provided by L. Jackson (personal communication, 2023) for 1993–2021.

2.4 State estimate

ECCO is a state estimate that combines the MIT general circulation model and most of available satellite and in situ data to produce a physically consistent estimate of the global ocean using an adjoint-based four-dimensional data assimilation system which optimizes the solution through adjusting initial conditions and parameters (including surface fluxes, wind stresses, and mixing parameters) (Fukumori et al., 2018). Here, we used monthly-averaged potential temperature, salinity and velocity fields from ECCO V4r4 on the native grid. ECCO V4r4 covers the time period from 1992 through 2017 and has a resolution of 1° in the horizontal and 50 irregularly spaced vertical levels. The reader is referred to Jackson et al. (2016; 2019) for a discussion of North Atlantic circulation features derived from GloSea5 reanalysis and ECCO state estimate and their comparison with other analyses.

2.5 Sea surface height

The daily altimeter sea surface height data from the Merged Absolute Dynamic Topography of Ssalto/Duacs AVISO (Archiving, Validation and Interpretation of Satellite Oceanographic data center) distributed by CMEMS on a 1/3° grid were interpolated on the OVIDE line grid. We used the monthly surface geostrophic velocities perpendicular to the OVIDE line that were computed for 1993–2021 from these sea surface heights.

2.6 NCEP atmospheric reanalysis

The 6-hourly wind stress data of the global atmospheric National Centers for Environmental Prediction (NCEP) / National Center for Atmospheric Research (NCAR) reanalysis (Kalnay et al., 1996) were linearly interpolated to the locations of the OVIDE line. We used monthly Ekman transports perpendicular to the OVIDE line that were then calculated for the time period 1993–2021.

3 Methods

3.1 Determination of absolute velocities for OVIDE hydrographic lines, CORA and EN4

For each occupation of the OVIDE hydrographic line over the period 2002-2021 and for the 1997 FOUREX line, the MOC was calculated using an inverse model constrained by volume conservation. The inverse model was described by Lherminier et al. (2007); the main steps of the method can be summarized as follows. Geostrophic velocities are obtained by combining geostrophic shears calculated from temperature and salinity observations measured at hydrographic stations with currents measured at the time of the cruise by SADCP (Ship-mounted Acoustic Current Profilers). The Ekman transport estimated from

NCEP is included in a surface layer (0–30 m). The inverse model calculates a correction to be applied to each pair of hydrographic stations to satisfy volume conservation (see also Lherminier et al., 2010; Gourcuff et al., 2011; Mercier et al., 2015; Zunino et al., 2017).

For the objective mappings CORA and EN4, the 0–2000 m geostrophic velocity was first computed at any point of the OVIDE line grid by combining the surface-referenced geostrophic current shears computed from CORA v5.2 or EN4 4.2.2 fields and surface geostrophic velocities obtained from altimetry. An Ekman velocity equal to the Ekman transport calculated from NCEP divided by the thickness of the shallower vertical layer was then added to the geostrophic velocity at this level. The method follows that of Mercier et al (2015) which can be referred to for further details.

3.2 MOC estimation

In the North Atlantic subpolar gyre, the water mass transformation from the upper to the lower branch of the AMOC takes place through progressive cooling of the winter mixed layer along the cyclonic subpolar gyre circulation, so that the upper and lower branches of the AMOC overlap in depth. The AMOC strength must therefore be calculated in density coordinates to capture all the associated water mass conversion (Lherminier et al., 2007; Mercier et al., 2015; Lozier et al., 2019). The MOC in density coordinate across the OVIDE line $\psi(t)$ reads:

$$\psi(t) = \int_{surface}^{\sigma_{moc}} \int_{Portugal}^{Greenland} v(x, \sigma, t) \, dx \, d\sigma, \tag{1}$$

where σ is potential density referenced to 1000 db, x is along-section distance, t is time, $\sigma_{moc}(t)$ is the density at the maximum of the MOC stream function $\psi(\sigma, t)$. σ_{moc} defines the isopycnal that separates the upper and lower limbs of the MOC. $v(\sigma, x, t)$ is the gridded velocity field perpendicular to the OVIDE line grid. $\psi(t)$ was calculated for all datasets, the OVIDE hydrographic sections (ψ_{hydro}), the CORA and EN4 objective analyses (ψ_{cora}, ψ_{en4}), the GloSea5 reanalysis ($\psi_{glosea5}$) and the ECCO state estimate (ψ_{ecco}). In the following, we will use the term "analyses" to refer to all these products, without singling out any one in particular.

The MOC strength was calculated by integrating $\psi(\sigma, t)$ from surface down to its maximum. The reason for not integrating from the bottom as usually done (Lherminier et al., 2007) is that CORA is only available for 0–2000 m, and integration from the surface means that we can use the same method for all analyses. The Arctic volume budget imposes a net northward transport across the OVIDE line which has been estimated at 0.8 Sv (1 Sv = 10^6 m^3 s^{-1}) on average from OVIDE inversions (Mercier et al., 2015). Here, positive transports are directed northward. This transport occurs in the upper branch of the MOC that therefore has a strength that is greater than that of the lower branch by the value of this net transport. A net northward transport is also present in ECCO and GloSea5 with a time-averaged value of 0.2 and 1.6 Sv respectively (Fig. S1). Unlike ECCO, whose net transport is relatively stable on decadal time scales, GloSea5 shows an increase in net transport of ~1Sv between the end of the 2000s and the end of the 2010s.

3.3 MOC decomposition

The aim of this section is to propose a decomposition of the MOC strength that decouples the time variations in MOC strength due, on the one hand, to changes in the volume of the upper layer of the MOC due to the variability in σ_{moc} and, on the other hand, to changes in velocity. We start by decomposing the MOC $\psi(t)$ into a time-averaged component $\bar{\psi}$ and a time-dependent component $\psi'(t)$ where the overbar denotes the time mean and the prime the variability about the time mean, following Desbruyères et al. (2013). For that purpose, we expand $v(\sigma, x, t)$ as:

$$v(z, x, t) \; = \; \bar{v}(z, x) + v'(z, x, t), \tag{2}$$

210

and define

$$\bar{\psi} = \int_0^{\overline{\sigma_{moc}}} \int_{Greenland}^{Portugal} \bar{v}(\sigma, x) \, dx \, d\sigma \tag{3}$$

215 where $\overline{\sigma_{moc}}$ is the time-averaged density of the maximum of the overturning stream function.

$\psi(t)$ can be written as well as:

$$\psi(t) = \int_0^{Z\sigma_{moc}} \int_{Portugal}^{Greenland} v(x, z, t) \, dx \, dz, \tag{4}$$

220

where z is depth and $Z\sigma_{moc}(x, t)$ is the depth of σ_{moc}, computed using the monthly density field along the section. It follows that the time averaged MOC can be rewritten as

$$\bar{\psi} = \int_0^{Z\overline{\sigma_{moc}}} \int_{Greenland}^{Portugal} \bar{v}(z, x) \, dx \, dz, \tag{5}$$

225

where $Z\overline{\sigma_{moc}}$ is computed using the time-averaged density field along the section. It follows that

$$\psi'(t) = \int_0^{Z\overline{\sigma_{moc}}} \int_{Greenland}^{Portugal} v'(z, x, t) \, dx \, dz + \int_{Z\overline{\sigma_{moc}}}^{Z\sigma_{moc}} \int_{Greenland}^{Portugal} \bar{v}(z, x, t) \, dx \, dz \; \ldots$$

230
$$+ \int_{Z\overline{\sigma_{moc}}}^{Z\sigma_{moc}} \int_{Greenland}^{Portugal} v'(z, x, t) \, dx \, dz, \tag{6}$$

or

$$\psi'(t) = \psi'_v(t) + \psi'_{\sigma_{moc}}(t) + \psi'_{v\,\sigma_{moc}}(t). \tag{7}$$

235

ψ'_v is the contribution to the MOC variability due to the time variability of the velocity field in the density layer bounded by the constant isopycnal limit $\overline{\sigma_{moc}}$. $\psi'_{\sigma_{moc}}$ is the contribution to the MOC variability due to the time change in the lower limit in density of the MOC upper limb or, in other words, to the change in volume of the upper limb of the MOC acting on the mean velocity field. A change in volume will be all the more effective in producing an MOC strength anomaly if it occurs in a region

240 where the mean current is strong (e.g. NAC or EGC). $\psi'_{v\,\sigma_{moc}}$ is the variability due to the correlation between the velocity fluctuations and the fluctuations in the depth of σ_{moc}. Note that $\psi_{Ekman}(t)$, the Ekman transport perpendicular to the section and integrated from coast to coast along the section, is included in the velocity component. The decomposition in Eq. 7 is exact, and we have verified that in our computations the sum of the three terms plus the mean is strictly equal to the MOC time series.

245 3.4 **Determination of seasonal cycle and statistics**

The statistics were calculated by considering the time series as a series of N correlated samples whose effective number of degrees of freedom is given by N/2τ where τ is the integral time defined from the auto-correlation function of the time series

calculated after subtracting the non-random components which are the mean, the trend and the average seasonal cycle of the series (Thomson and Emery, 2014). The confidence interval on the cross-correlation coefficient r between two time series a and b was calculated by noting that $\ln[(1+r)/(1-r)]$ is a Gaussian random variable (see Thomson and Emery, 2014). The effective number of degrees of freedom for the cross-correlation r was calculated following Bretherton et al. (1999) and is given by $N(1-r_a r_b)/(1+r_a r_b)$ where r_a and r_b are the values of the lag 1 auto-correlations of the a and b series.

Time series trends were determined by least-squares fitting of a first-order polynomial to the observations. The trend error was determined as the standard deviation of a set of 2,000 trend estimates calculated from perturbed time series obtained by randomly permuting blocks of least-squares adjustment residuals. This method, known as moving block bootstrap (MBB) resampling (Mudelsee, 2019), uses blocks of residuals whose length depends on the temporal correlation between the residuals and which therefore preserve the correlation between the residuals during permutation.

The seasonal cycle of the time series was obtained by removing the trend, then applying a high-pass filter with a cut-off frequency of two years, then averaging the high-pass filtered time series variable for each calendar month separately. The standard error was calculated as the ratio of the intra-annual standard deviation divided by the number of degrees of freedom on the assumption that MOC observations for a given month one year apart are independent.

4 Results

4.1 MOC time series

Time series of MOC strength $\psi(t)$ show for all the analyses an energetic seasonality as well as a smaller but discernible inter-annual to decadal variability (Figure 2). Over the period 1993-2021, the mean values of ψ_{cora} (19.7±0.4 Sv), ψ_{en4} (20.3±0.4 Sv) and $\psi_{glosea5}$ (20.0±0.3 Sv) are close with overlapping standard errors (Table 1). ψ_{cora} and ψ_{en4} have a small bias with respect to ψ_{hydro}, the MOC strengths obtained by analysis of the OVIDE hydrographic lines (-0.23±0.8 and 0.23±0.7 Sv, respectively, see Table 1). These biases are for the June-July period, when the cruises were carried out, with the sole exception of the 1997 cruise carried out in September. $\psi_{glosea5}$ overestimates the MOC strength compared with ψ_{hydro} by 2.75±0.7 Sv. ψ_{cora} and ψ_{en4} show very similar signals with the exception of certain winters with marked differences in MOC strength (e.g. 2014). These two analyses are positively correlated (r = 0.63, Table 2). $\psi_{glosea5}$ shows correlations of 0.22 and 0.17 with ψ_{cora} and ψ_{en4}, respectively (Table 2). Although significantly different from zero at the 99% confidence level, these correlations are weaker than those between ψ_{cora} and ψ_{en4} and reflect, despite broadly similar multi-year variability, differences at intra-annual frequencies (e.g. 2006 to 2009, Figure 2). The mean value of ψ_{ecco} (15.2±0.4 Sv) is significantly lower than those of ψ_{cora}, ψ_{en4} and $\psi_{glosea5}$. This is not primarily due to the different periods under consideration, as for the period covered by ECCO ψ_{ecco} is lower than ψ_{hydro} by -2.95±0.7 Sv on average (Table 1). In brief, the analyses show a bias with hydrography that is positive for GloSea5, and negative for ECCO and a good agreement between hydrography, EN4 and CORA. It should be noted that the MOC strength estimates from the four analyses are not independent, as they are based on largely similar data sets (altimetry, Argo and ship-based hydrography). However, none of them assimilates the S-ADCP data that are decisive in estimating ψ_{hydro} (Lherminier et al., 2007).

The spatial evolution of the cumulated transport of the upper limb of the MOC from Greenland to Portugal, averaged over the duration of the hydrographic cruises, provides a better understanding of the origin of the biases observed in the restitution of the MOC by the different analyses (Figure 3). GloSea5 has a larger bias with ψ_{hydro}, but shows the closest match to hydrographical observation regarding the along-section transport distribution, except for the presence of a ~2 Sv northward eastern boundary

current, which at that time of the year is not present in the hydrography, the objective analyses or the state estimates. Overall, there is a good agreement between CORA, EN4 and the hydrography, even though the objective analyses show a more intense NAC transport than that observed during the cruises. The ECCO state estimate shows a lower NAC transport than in the observations, which is the main cause of a lower AMOC strength compared to the hydrography.
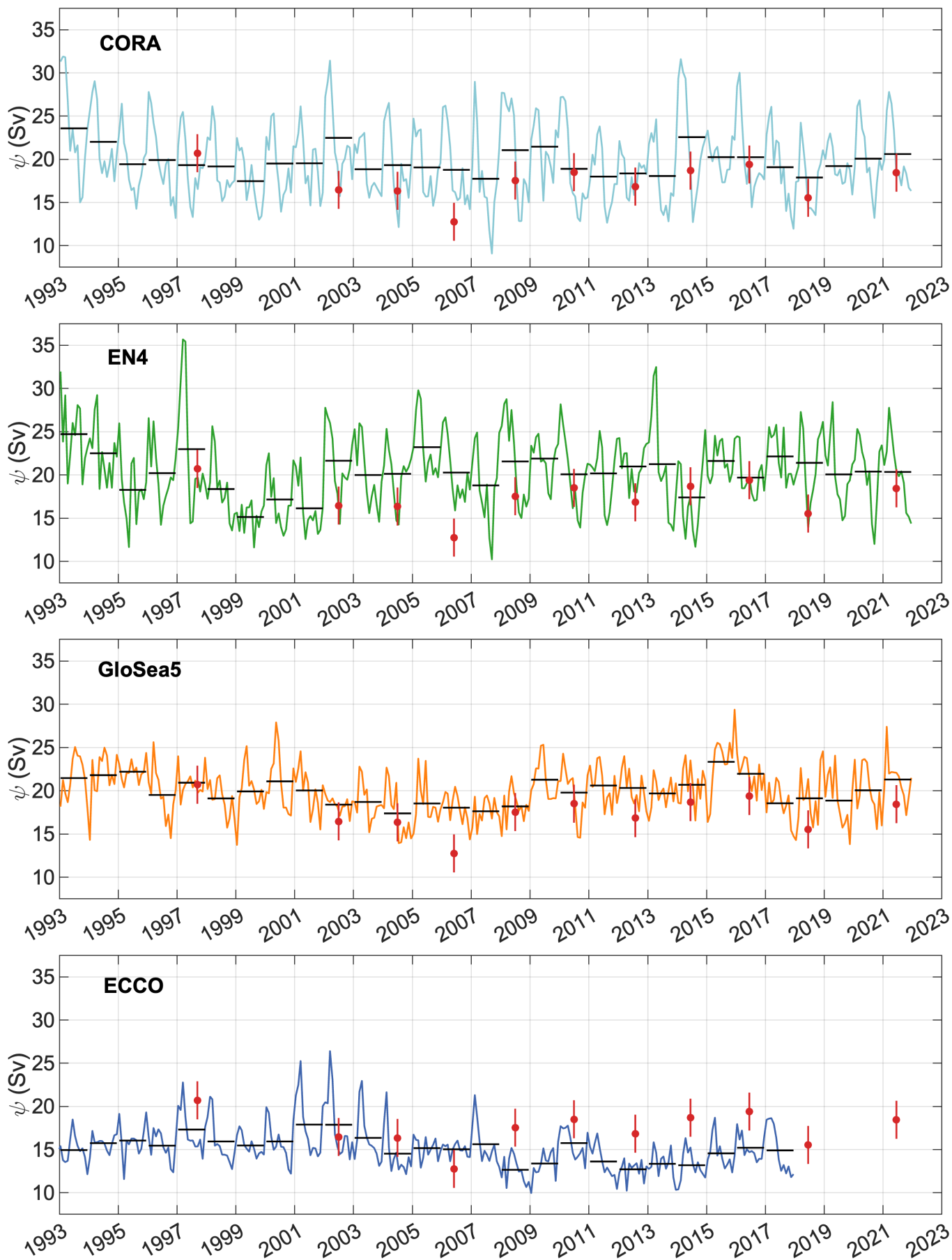
Figure 2: Time series of MOC strength at OVIDE from CORA (light blue), EN4 (green) and GloSea5 (orange) and ECCO (blue) in Sv. MOC strengths and associated standard errors estimated from OVIDE hydrographic lines are plotted in red. The annual means of each time series (black, horizontal lines) are also indicated.

295

	$\langle MOC \rangle$	std(MOC)	std(MOC_{intra})	rms(MOC) with hydro	$\langle \sigma_{moc} \rangle$	std(σ_{moc})	rms(σ_{moc}) with hydro
CORA	19.7±0.4	4.3	4.0	2.6 (-0.23±0.8)	32.18	0.07	0.06 (0.02)
EN4	20.3±0.4	4.3	3.7	2.2 (0.23±0.7)	32.19	0.07	0.06 (0.04)
GloSea5	20.0±0.3	2.7	2.3	2.4 (2.75±0.7)	32.17	0.08	0.05 (0.04)
ECCO	15.2±0.4	2.5	2.0	2.3 (-2.95±0.7)	32.16	0.08	0.04 (0.01)
hydro	17.4±0.6	2.1		0 (0)	32.15	0.03	0 (0)

Table 1: Statistics for MOC strength time series in Sv and σ_{moc} time series in kg m⁻³: Mean ($\langle \bullet \rangle$), standard deviation (std($\bullet$)), and root mean square differences with estimates from OVIDE hydrography rms($\bullet$). The standard error is reported for $\langle MOC \rangle$. Biases with respect to hydrography are reported in parentheses in the rms columns. MOC stands for MOC strength, MOC_{intra} for the intra-annual component of the MOC strength and hydro refers to estimates from OVIDE line repeated hydrography.
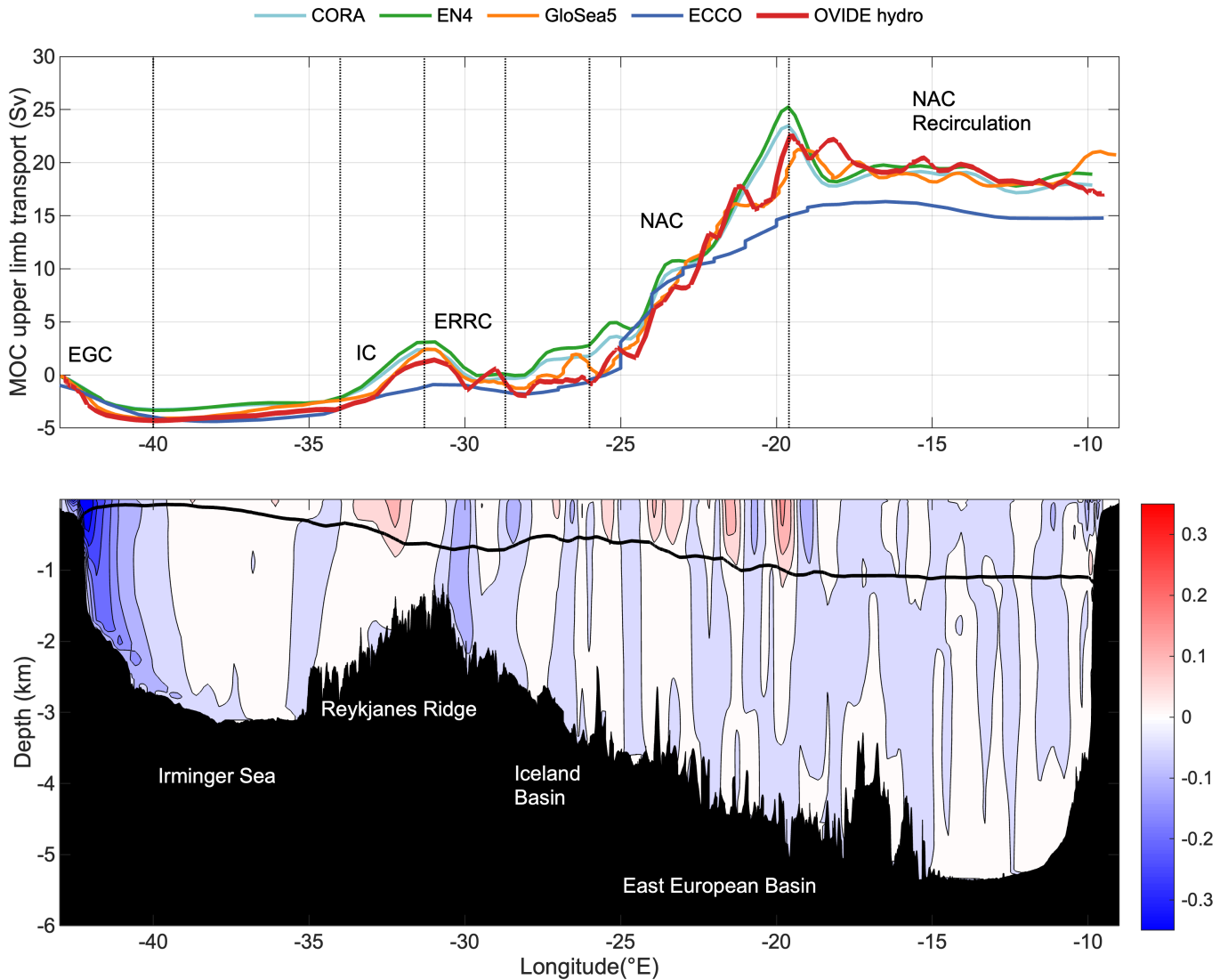
Figure 3: (upper panel) Cumulated transport from Greenland to Portugal along the OVIDE line in the MOC upper limb in Sv for CORA (light blue), EN4 (green), GloSea5 (orange) and ECCO (blue) averaged over the time period covered by the cruises, and the average of the 1997–2018 OVIDE hydrographic line (red). (lower panel) geostrophic velocity (m s⁻¹) perpendicular to the OVIDE line averaged over the OVIDE cruises and adapted from Daniault et al. (2016). Positive velocities indicate that the meridional component of the current is directed northwards. The continuous black line is σ_{moc} averaged over the OVIDE cruises. Main bathymetric features are indicated. EGC stands for East Greenland Current, IC for Irminger Current, ERRC for East Reykjanes Ridge Current, NAC for North Atlantic Current, with the dotted vertical lines indicating the extension in longitude of the currents.
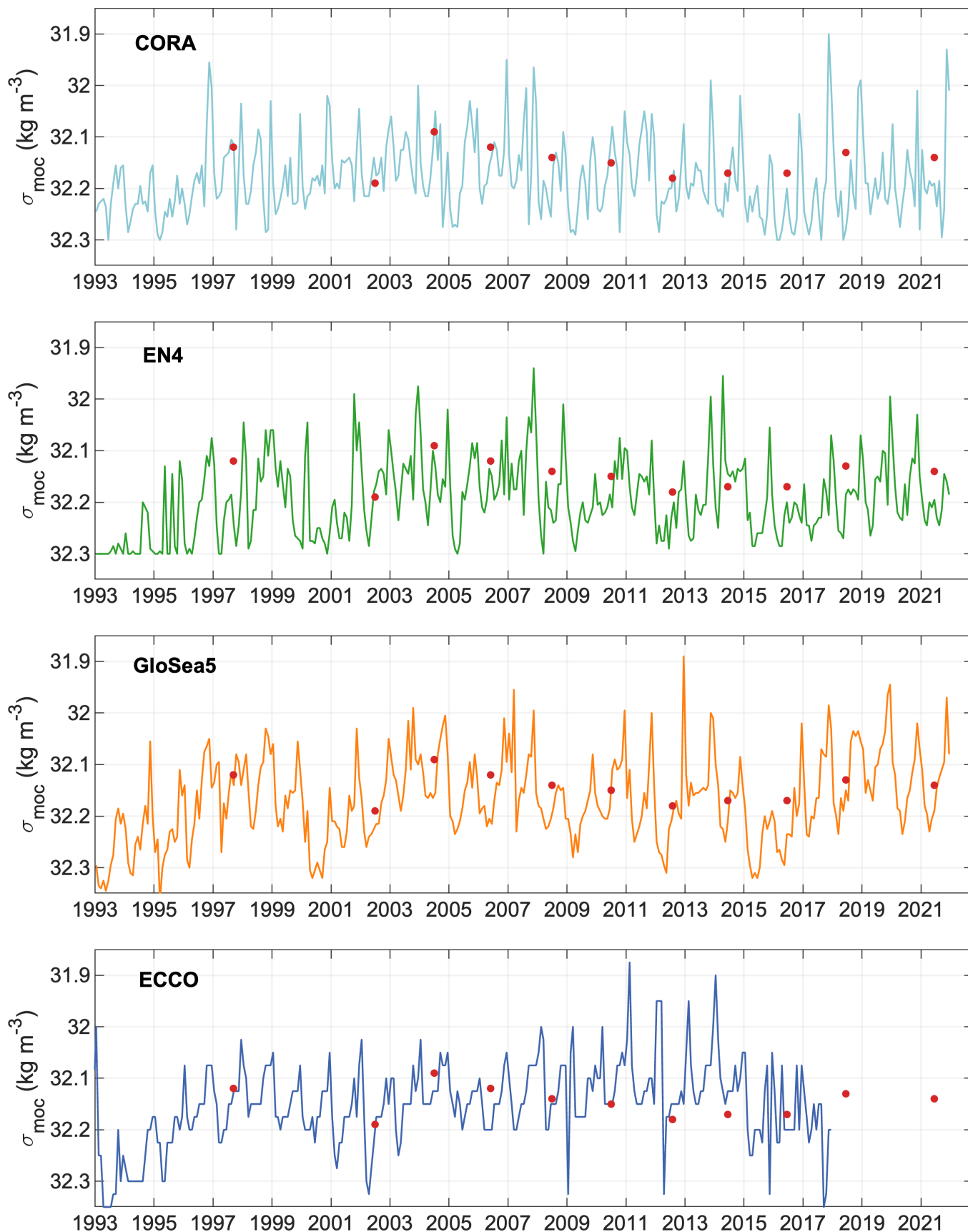
Figure 4 : Times series of potential density reference to 1000 dbar at the maximum of the overturning stream function (σ_{moc}) in kg m^{-3} for CORA (light blue), EN4 (green) and GloSea5 (orange) and ECCO (blue). σ_{moc} from OVIDE hydrographic lines are plotted as red dots.

The MOC annual average in Figure 2 shows a decreasing MOC in the 1990s and early 2000s for ψ_{cora}, ψ_{en4} and $\psi_{glosea5}$, more pronounced for ψ_{en4}. For ψ_{cora} and $\psi_{glosea5}$, this is followed by a period of lower MOC between 2000 and 2008 and a period of MOC fluctuations around a higher mean until 2021. ψ_{en4} fluctuates around a high MOC value from 2003 onwards. The annual mean from ψ_{ecco} shows a decrease in MOC from the early 2000s to the late 2010s, with inter-annual variability superimposed (Figure 2d). In the late 2010's, the average annual of ψ_{ecco} is below 15 Sv. It is over this last period that the negative bias in regard to ψ_{hydro} is most noticeable. Trends were calculated for the different time series over their entire duration, but none were significant at the 95% confidence level and they are not described here. The magnitude of MOC strength variability is measured by the standard deviation of the time series (Table 1). With a standard deviation equal to 4.3 Sv, ψ_{cora} and ψ_{en4} show significantly more variability than $\psi_{glosea5}$ (standard deviation of 2.7 Sv) and ψ_{ecco} (2.5 Sv) (Table 1). For each analysis, the intra-annual component largely explains the intensity of the variability (Table 1). The differences between the standard deviations are therefore mainly due to differences in seasonal signal amplitude.

Time series of σ_{moc} show strong intra-annual variability superimposed on interannual to decadal variability (Figure 4). During an intra-annual cycle, σ_{moc} is at its densest at the end of winter. σ_{moc} has an average value of between 32.16 and 32.19 kg m^{-3} depending on the analysis considered (Table1). All the analyses show that the densest value of $\sigma_{moc} \sim 32.25$ kg m^{-3} occurred in the early 1990s. Then, σ_{moc} gradually decreased to reach 32.1 kg m^{-3} in the mid-2000s to become again denser ~ 32.2 kg m^{-3} in 2015-2016. σ_{moc} follows the trends of the subpolar gyre, which became less dense (warming) between the mid-1990s and 2006, then became denser (cooling) until 2016, and has been warming again since then (Desbruyères et al., 2015, 2021). Higher frequency inter-annual variability is superimposed on this decadal cycle.

	EN4	GloSea5	ECCO
CORA	0.63	0.22	0.34
EN4		0.17	0.23
GloSea5			0.28

Table 2: Cross-covariances of MOC time series in Sv (all reported cross-covariances are significantly different from zero at the 99% confidence level).

	$std(\psi'_v)$	$std(\psi'_{\sigma_{moc}})$	$std(\psi'_{v\,\sigma_{moc}})$	$std(\psi'_{Ekman})$
CORA	2.56	3.17	0.92	
EN4	2.70	3.33	0.94	
GloSea5	2.12	2.21	0.91	
ECCO	1.18	1.94	0.42	
NCEP				1.40

Table 3: Standard deviations of MOC decomposition terms (Eq. 7 and following discussion) reported in Sv.

4.2 MOC decomposition

We decomposed the MOC strength time series according to equation 7. ψ'_v and $\psi'_{\sigma_{moc}}$ for the four analyses are shown in Figure 5 and 6 respectively; the associated statistics are presented in Table 3. The two components ψ'_v and $\psi'_{\sigma_{moc}}$ contribute to the interannual to decadal MOC variability, whereas $\psi'_{\sigma_{moc}}$ explains most of the seasonality of the MOC strength, which is confirmed by a spectral analysis (Figure S2). The variance due to velocity fluctuations amounts to 37 % (ECCO), 65.2 % (CORA), 66.9 % (EN4) and 92% (GloSea5) of the variance due to σ_{moc} depth variations. Variability in the depth of σ_{moc} is therefore the dominant mechanism for generating variance in the subpolar MOC. It is worth noting that, as we shall see below,

this result is representative of the seasonal scale, which is the time scale that predominates in the variability spectrum, but not of
350 the inter-annual to decadal scales. The contribution of the coupled term $\psi'_{v\,\sigma_{moc}}$, which represents the correlation between
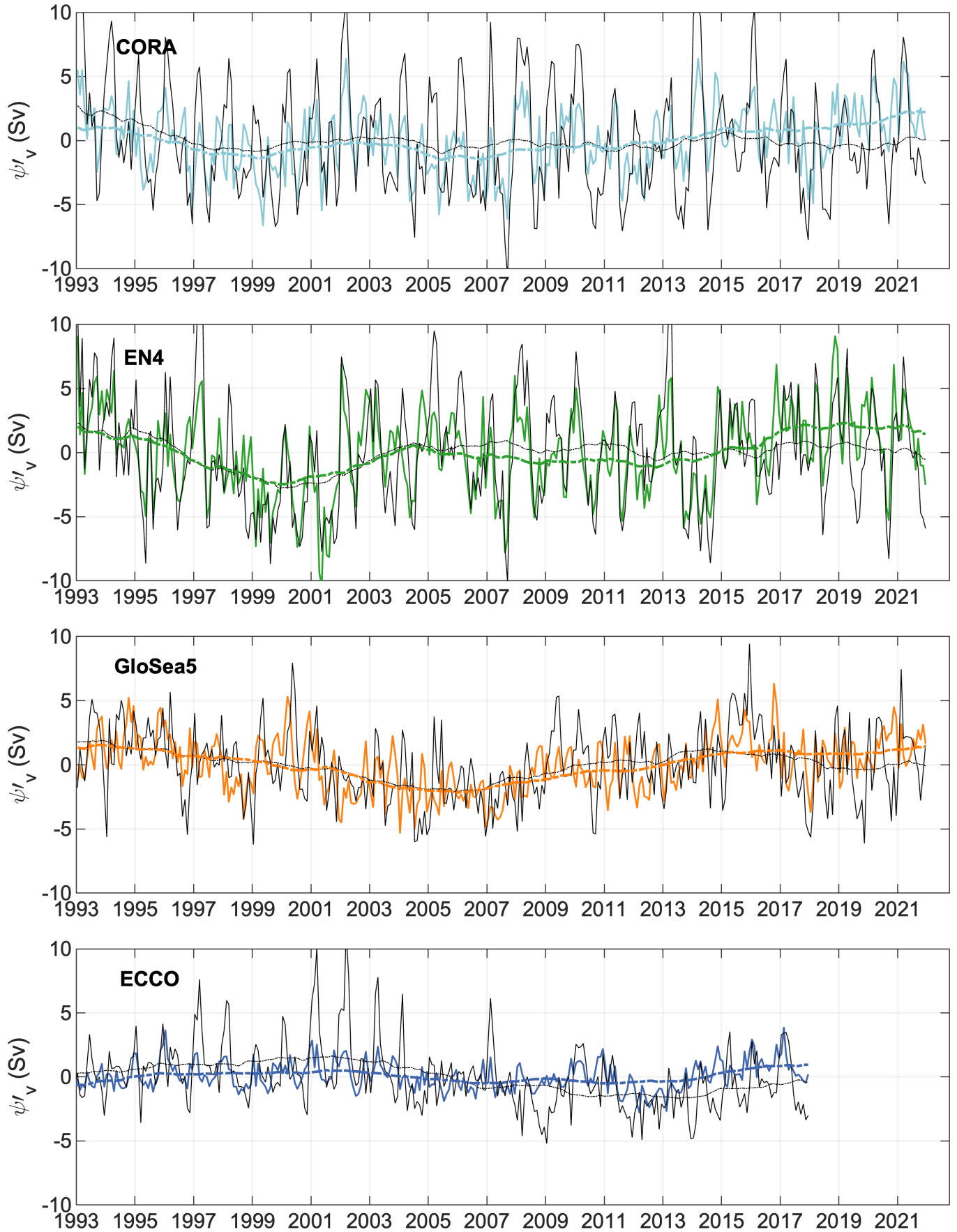
Figure 5 : Coloured solid lines are times series of ψ'_v in Sv for CORA (light blue), EN4 (green), GloSea5 (orange) and ECCO (blue). The black solid lines are ψ'. The coloured (black) dashed lines are ψ'_v (ψ') after low-pass filtering with a moving average of 60 months.
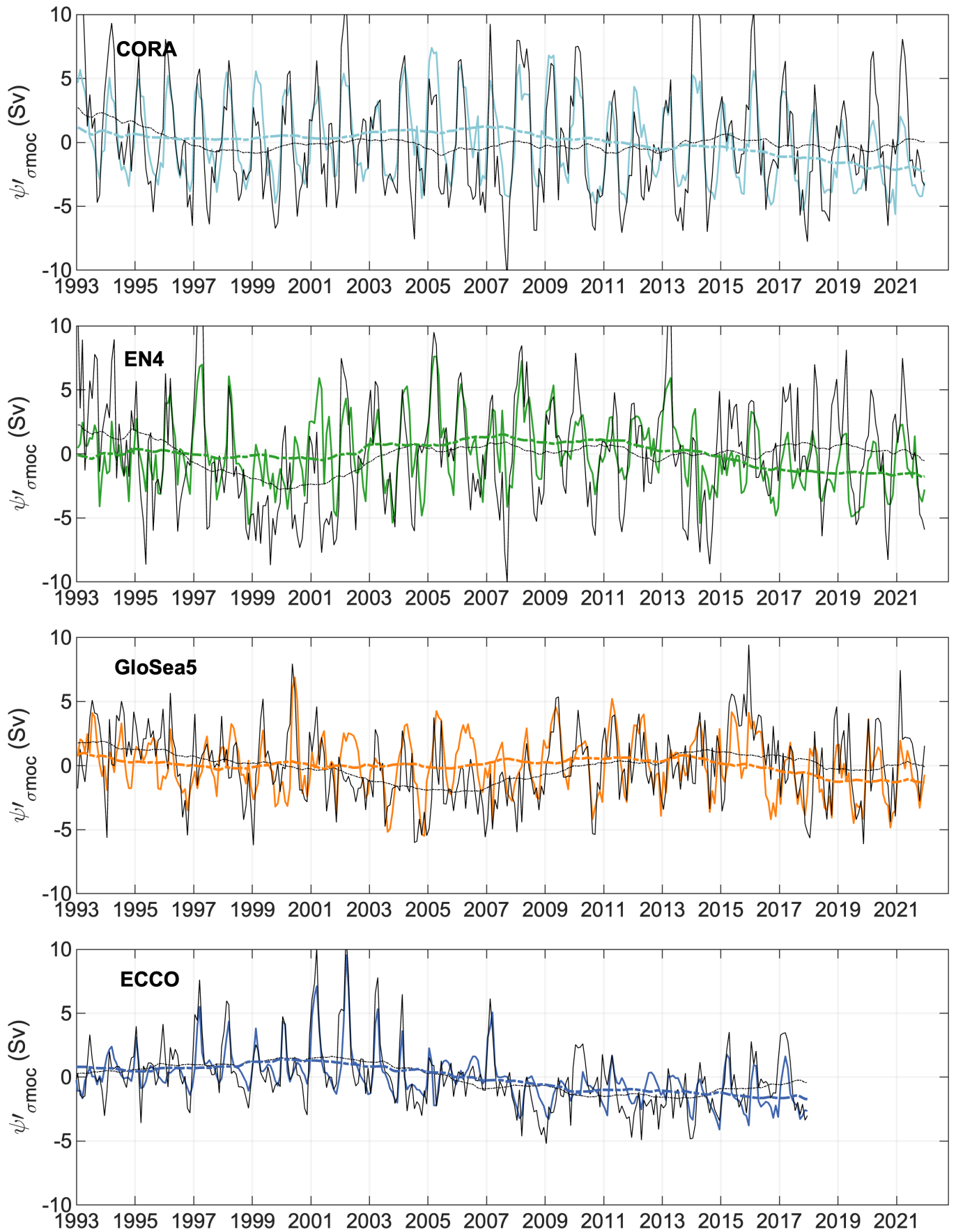
Figure 6 : Coloured solid lines are times series of $\psi'_{\sigma_{moc}}$ in Sv for CORA (light blue), EN4 (green), GloSea5 (orange) and ECCO (blue). The black solid lines are ψ'. The coloured (black) dashed lines are $\psi'_{\sigma_{moc}}$ (ψ') after low-pass filtering with a moving average of 60 months.

velocity fluctuations and σ_{moc} depth fluctuations, explains less than 10% of the variance. The variance of Ekman transport is included in ψ'_v and accounts for 18% (EN4), 19.5% (CORA), 40% (GloSea5) and 52.1% (ECCO) of the variance of $\psi'_{\sigma_{moc}}$. Note that these percentage variations therefore only reflect variations in the amplitude of $\psi'_{\sigma_{moc}}$ as here we estimate ψ'_{Ekman} from NCEP regardless of the analysis considered. The variability of ψ'_{Ekman} and $\psi'_{v\,\sigma_{moc}}$ is mainly at sub-seasonal frequencies (Figure S2). In what follows, we focus on seasonal and decadal time scales.

	$< \psi'\psi'_v >$	$< \psi'\psi'_{Z\sigma_{moc}} >$	$< \psi'_v\psi'_{Z\sigma_{moc}} >$
CORA	**0.41**	0.22	**-0.78**
EN4	**0.75**	0.13	**-0.54**
GloSea5	**0.88**	0.21	-0.26
ECCO	**0.41**	**0.90**	-0.00

Table 4: Correlation between the two leading terms of the MOC decomposition ψ'_v and $\psi'_{Z\sigma_{moc}}$ and the MOC strength for the 60-month moving mean low-passed filtered time series. Correlations statistically different from zero at the 95% confidence level are reported in bold.

4.3 Seasonality

The MOC seasonal cycle at OVIDE is relatively consistent between the analyses (Figure 7a). The seasonal cycle of ψ peaks in March, except for GloSea5 that peaks in late spring, and it troughs between July and October for CORA, EN4 and GloSea5, and November for ECCO. The peak-to-trough amplitude of the seasonal cycle varies by a factor of two between the analyses, from 8 ± 0.92 Sv for ψ_{CORA}, which has the most intense seasonal cycle, to 3.7 ± 0.84 Sv for ψ_{ECCO}. The seasonal cycle of $\psi'_{\sigma_{moc}}$ is similar in amplitude and phase to that of ψ, which confirms that the main driver of the seasonality is the seasonal variation in the depth of σ_{moc} (Figure 7b). Velocity fluctuations ψ'_v contribute more marginally to the seasonal cycle of ψ, with an average seasonal cycle of ~ 2 Sv from peak to trough (Figure 7c). Overall, the seasonal cycle of ψ'_v, which is at its maximum in October–November and at its minimum in July, is offset when compared to the seasonal cycle of $\psi'_{\sigma_{moc}}$. In autumn, the two seasonal cycles are opposed; nonetheless, ψ'_v shows a secondary peak in March for CORA and EN4 that amplifies the late winter peak in ψ seasonal cycle. Ekman transport, which is included in ψ'_v, contributes to the seasonal cycle with a peak-to-trough amplitude of 1.7 Sv, with a minimum in November and a maximum in June (Figure 7a). The seasonal cycle of σ_{moc} is very similar in all analyses, with the densest values observed in April (+0.05 kg m^{-3} on average, Figure 7d) lagging the seasonal maximum of ψ by one month and the least dense values in December–January (-0.06 kg m^{-3} on average).

Panels a–d in Figure 8 show the variation in longitude of σ_{moc} depth between Greenland and Portugal for the extremes of the seasonal cycle. Consistently across all analyses, σ_{moc} is located at around 1000 m in the Iberian Basin, south-east of the NAC, rising westwards through the NAC to reach depths of ~200 m in the central Irminger Sea before deepening again in the EGC. In late winter–early spring, σ_{moc} is denser than during the rest of the year (Figure 7d). In the central Irminger Sea and in the EGC, upper layers densify in winter due to winter deep convection and subduction of convected water into the EGC (Piron et al., 2017; Le Bras et al., 2020). As a result, σ_{moc}, although denser in late winter, is found there at shallower depths in winter than in summer or autumn (Figures 7e,f and 8a–d). Elsewhere, and in particular in the NAC, which is the main supplier of northward transport in the MOC upper limb, σ_{moc} is found at a greater depth at its density maximum in April than during the rest of the year (Figures 7g and 8a–d). This is because, in the NAC system, there is no seasonal variation in density at the depth of σ_{moc} (not shown), and the seasonal variation in σ_{moc} density causes here a vertical shift in σ_{moc} depth according to the average density profile, which increases downwards. In brief, the volume of the upper branch of the MOC decreases between late autumn and late winter in the EGC and central Irminger Sea, while it increases elsewhere. As in first approximation, the northward transport in the upper

branch of the MOC is due to the NAC, partially offset by the southward transport in the EGC (Figure 3), this change in volume leads to an increase in the northward contribution of the NAC and a decrease in the southward contribution of the EGC to the upper MOC transport. Figure 8e shows that, with the exception of GloSea5, it is the transport anomaly in the EGC that makes the strongest contribution to the $\psi_{\sigma_{moc}}$ seasonal amplitude anomaly, complemented by the transport anomaly in the NAC (transport anomalies in the Irminger Current and the East Reykjanes Ridge Current mostly balance each other out). Overall, the MOC is more intense in winter than in summer or late autumn. It is therefore the deep convection events triggered by intense air-sea buoyancy loss and the eddy-driven subduction of the convected water into the EGC that drive significant variation in the depth of σ_{moc} and the volume-driven seasonal cycle of the MOC. Seasonality in ψ_v is dominated by that of the eastern boundary current, which is around 3 Sv more intense in October–November than in July–August (Figure 8f). Note that although the eastern
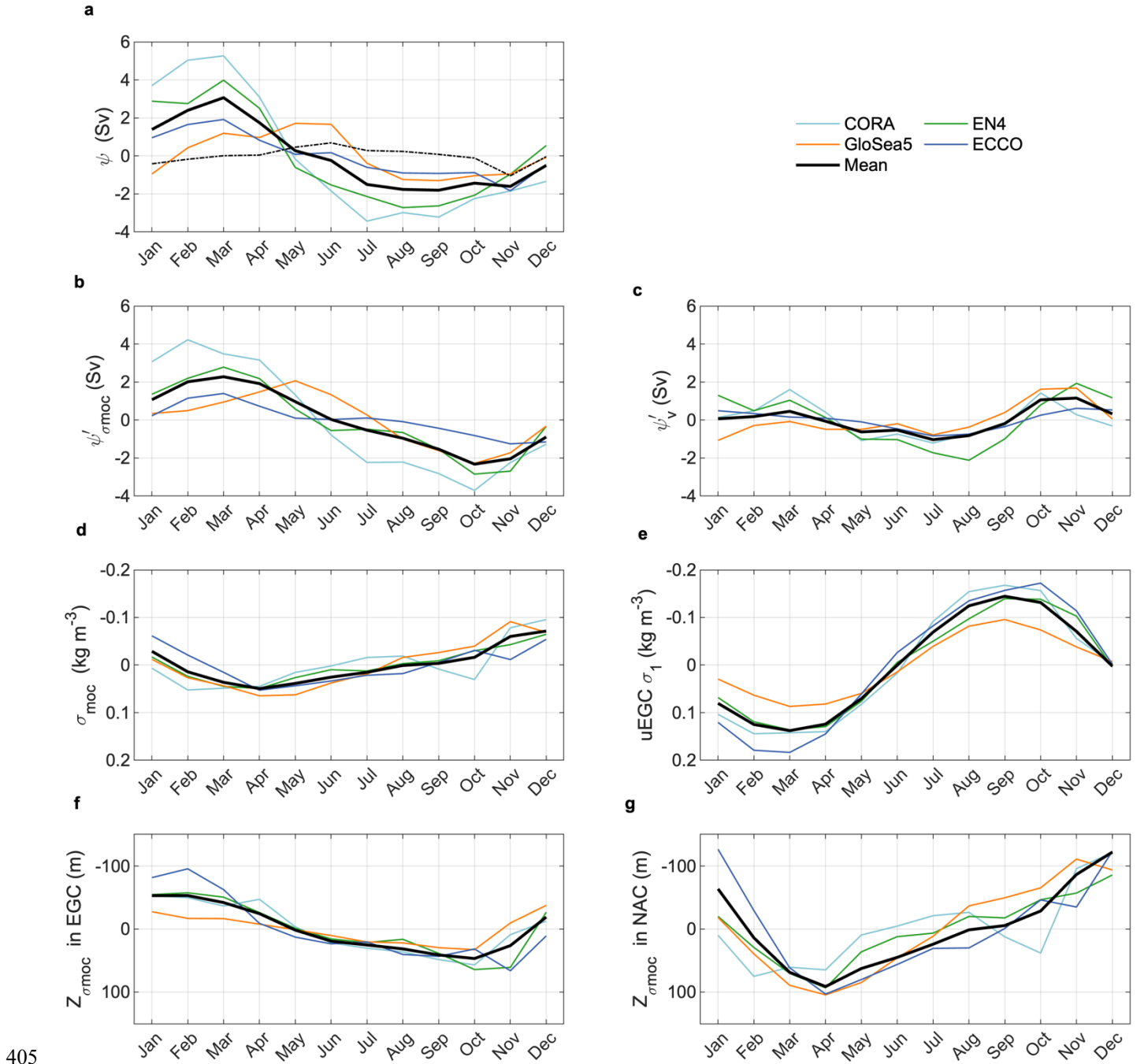
Figure 7 : Mean intra-annual variability of (a) MOC ψ' at OVIDE in Sv, (b) $\psi'_{\sigma_{moc}}$, (c) ψ'_v, (d) σ_{moc} in kg m^{-3}, (f) σ_1 in the upper EGC (100-300 m), (e) $Z_{\sigma_{moc}}$ in the EGC defined as the southward flowing western boundary current west of 40°W (Figure 3), (f) $Z_{\sigma_{moc}}$ in the NAC defined as the broad current system east of 26°W (Figure 3). Each panel shows CORA (light blue), EN4 (green), GloSea5 (orange), ECCO (blue) and the mean of all 4 analyses. Black-dashed line in (a) is the Ekman transport, common to all analyses.

boundary current in GloSea5 was more intense in June–July than in the other analyses (Figure 3), the amplitude of its seasonality between July–August and October–November is similar to that of the other analyses. The seasonality of the eastern boundary current counterbalances that of the EGC and the recirculation to the south of the NAC, east of 20°W, which are more intense in October–November, but are directed southwards and therefore tend to weaken the MOC (Figure 8f).
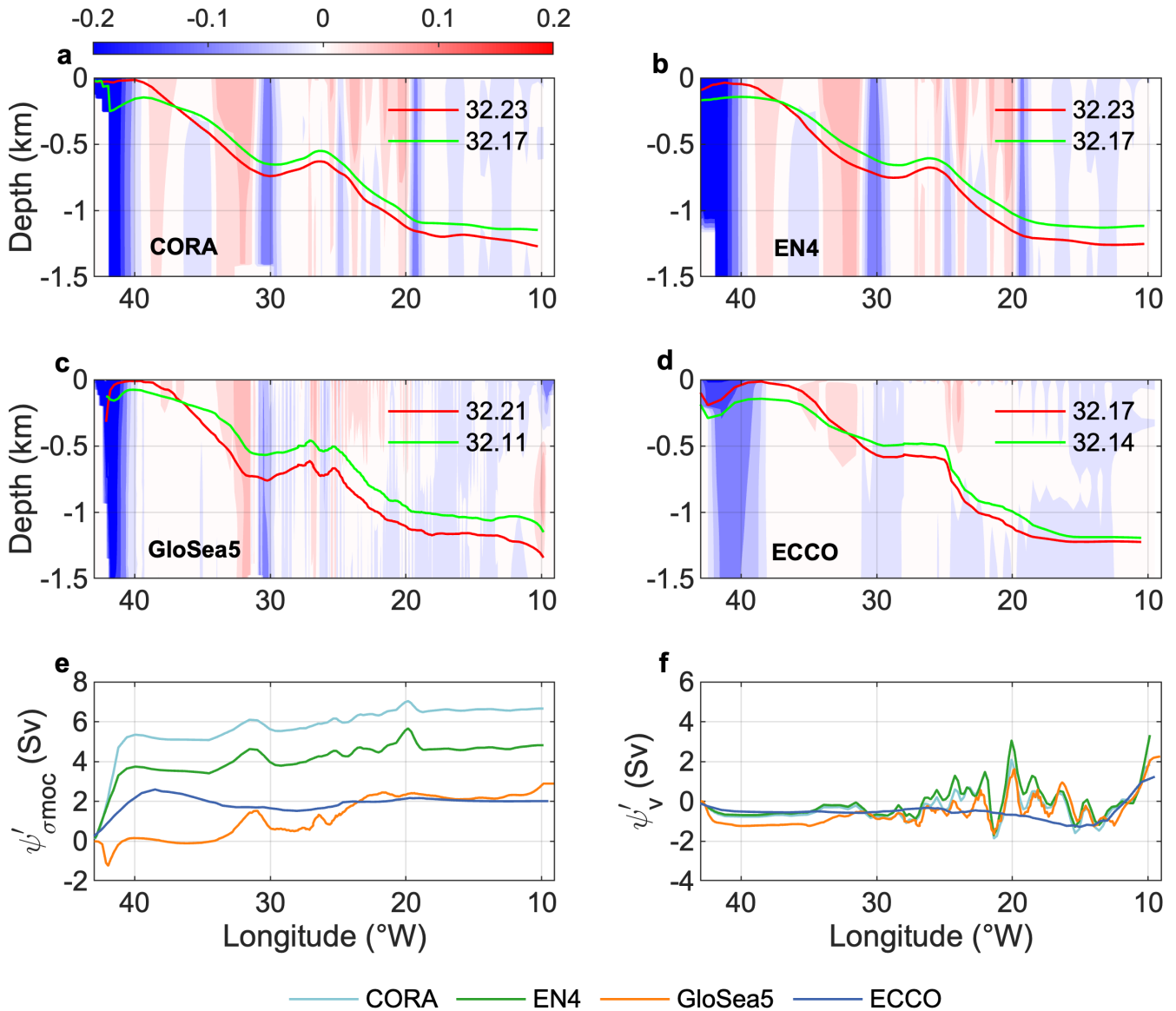
Figure 8 : The longitude evolution of σ_{moc} depths averaged over February–April (red, maximum of ψ seasonal cycle) and September–November (green, minimum of ψ seasonal cycle) for (a) CORA, (b) EN4, (c) GloSea5 and (d) ECCO from Greenland to Portugal. The background field is the velocity perpendicular to the OVIDE line in m s⁻¹. Legend in panels a-d is density of σ_{moc}. (e) Transport anomalies corresponding to the difference between the 3-month average at the maximum and minimum of $\psi'_{\sigma_{moc}}$ seasonal cycle (February–April minus September–November) for $\psi'_{\sigma_{moc}}$. (f) Transport anomalies corresponding to the difference between the 3-month average at the maximum and minimum of ψ'_v seasonal cycle (October–November minus July–August). Transport anomalies are reported in Sv and accumulated eastward from the Greenland coast in the upper limb of the MOC for $\psi'_{\sigma_{moc}}$ (e) and ψ'_v (f).

4.4 Decadal signal

On a decadal scale, studied here from low-pass filtered time series using a 60-month moving average, CORA, EN4 and GloSea5 show that the strength of the MOC at OVIDE decreased from 1993 until 1999 for CORA and EN4 and until 2006 for GloSea5 (Figures 5 and 6, black dotted lines). After a quick recovery, the analyses do not show any particular trends during the 2010s, except for a weak relative maximum in the middle of the decade for CORA and EN4. ECCO missed the MOC decline in the 1990s, which is most often identified in analyses (see e.g. Jackson et al., 2022), but like the other analyses shows no particular trend in the 2010s. In this section we study decadal variability based on the decomposition of section 4.2 and low-passed filtered time series (Figures 5 and 6). At these time scales, ψ'_v shows a positive correlation with ψ', significant at the 95% confidence

level for all analyses (Table 4, Figure 5). With the exception of ECCO, $\psi'_{\sigma_{moc}}$ is not significantly correlated with ψ'. The variability of the MOC at OVIDE on decadal timescales therefore appears mainly driven by velocity fluctuations. This is particularly true between 1993 and the mid-2000s (Figure 5). We note, however, that in all analyses, $\psi'_{\sigma_{moc}}$ decreases between
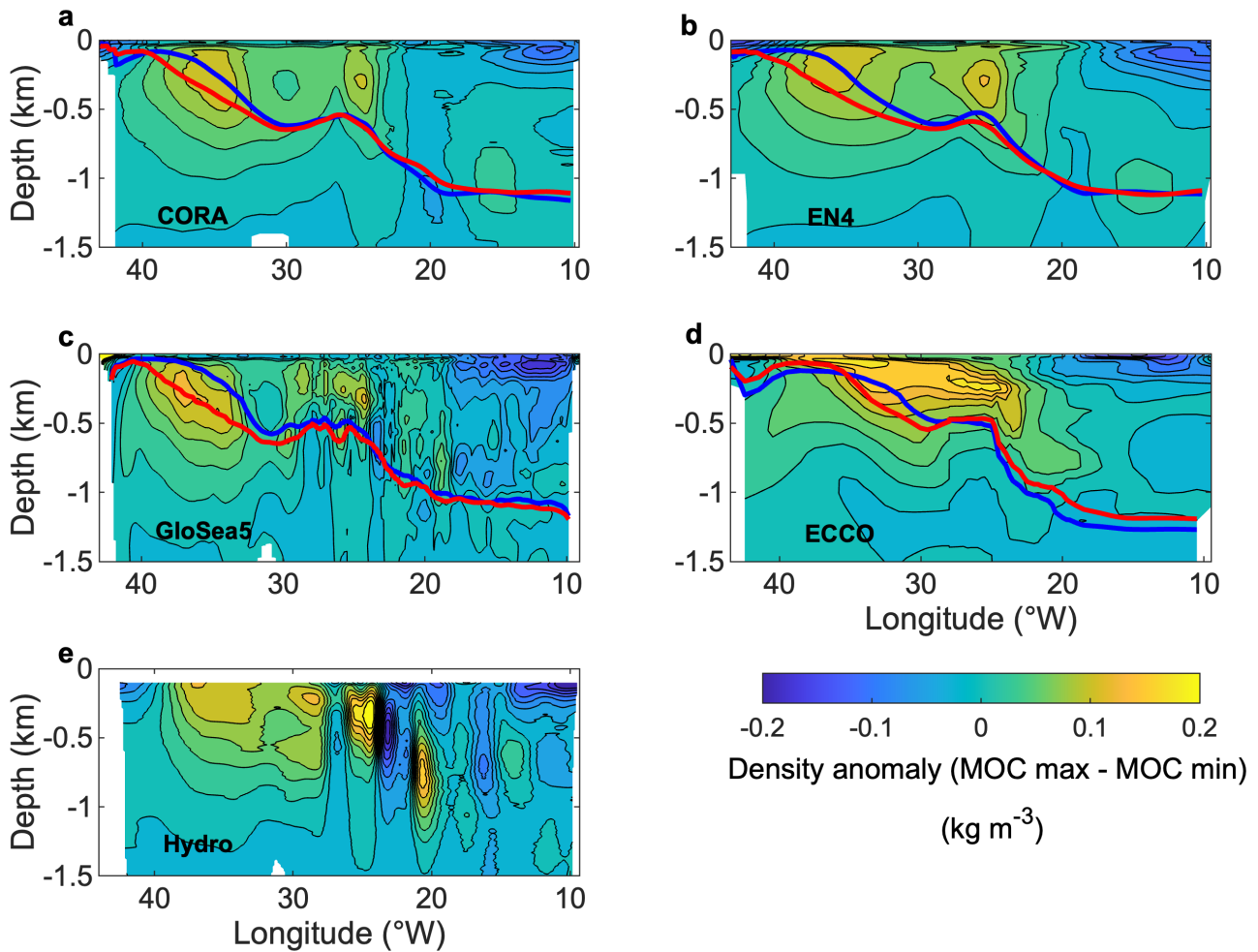
Figure 9: Density difference (kg m⁻³) between 2015–2018 and 2004–2008 for CORA (a), EN4 (b), GloSea5 (c), ECCO (d) and OVIDE hydrography (e) for 0-1500 m along the OVIDE line (Figure 1). The longitude evolution of σ_{moc} depths averaged over 2015–2018 (blue solid line) and 2004–2008 (red solid line) are superimposed for panels a - d. For the OVIDE hydrography, the density difference was calculated from the cruise data and smoothed horizontally using a moving average of 70 km to remove noise due to the snapshot nature of the data. Only the density difference for depths less than -0.1 km are plotted to avoid the seasonal aliasing affecting both the surface layer and the σ_{moc} depth.

the mid-2000s and the late 2010s, while ψ'_v increases over the same period (Figures 5 and 6). $\psi'_{\sigma_{moc}}$ and ψ'_v show opposite behavior and an anti-correlation computed over the entire time series lengths, significant at 95% confidence, for CORA and EN4. To better understand this anti-correlation, we examine in Figure 9 the density anomalies along the OVIDE section for 2015-2018 (maximum of MOC) compared to 2004-2008 (minimum of MOC). In CORA and EN4 (Figure 9 a–b), the signals show a densification broadly affecting the first 1000 meters west of the subpolar front at ~25°W, with local maxima in the center of the Irminger gyre and east of the Reykjanes ridge, and a lightening of the upper layers east of 20°W. Similar signals are also observed from OVIDE hydrography, which however present some eddying structures (e.g. between 20° and 25° W) due to the snapshot nature of the measurements (Figure 9e). These density anomalies result in a change in horizontal density gradients, an increase in geostrophic velocities east of 25°W and finally an increase in the northward transport in the upper branch of the MOC as observed in the MOC velocity-driven component ψ'_v east of 25°W (Figure 10). The densification of the upper branch of the MOC to the west of the subpolar front contributes to a raising σ_{moc} and results in a decrease in the volume of the upper branch of the MOC in the Irminger current (Figure 9). Therefore, the transport due to the volume-driven MOC component $\psi'_{\sigma_{moc}}$ decreases between the two periods (Figure 10). GloSea5 shows the same structure of the upper layer density anomaly as CORA

and EN4, but weaker (Figure 9a–c), and the same transport decadal variability for ψ'_v and $\psi'_{\sigma_{moc}}$ except in EGC for $\psi'_{\sigma_{moc}}$

455 (Figure 10). Interestingly, the ~4 Sv increase in ψ'_v appears to translate into a ~1Sv increase in net transport for GloSea5 (Figure S1). In ECCO, the positive density anomaly is intensified (Figure 9d) compared to the density anomalies in the other analyses, and it appears subducted towards the south-east, below the subpolar front and in the thermocline, in disagreement with the other analyses. This results in a change in the horizontal density gradients and explains the different behavior of the state estimate (Figure 10). Overall, the variability of the MOC at OVIDE on decadal time scales results from the opposite behavior of ψ'_v and

460 $\psi'_{\sigma_{moc}}$, each of which depends on the way the analysis reproduces the anomalies in the density field. For the objective analyses CORA and EN4 and the reanalysis GloSea5, whose MOC reconstructions are in good agreement with observations from the OVIDE line (Figure 2), the ψ'_v anomaly is about twice the $\psi'_{\sigma_{moc}}$ anomaly, which explains why the entire MOC variation appears driven by velocity.
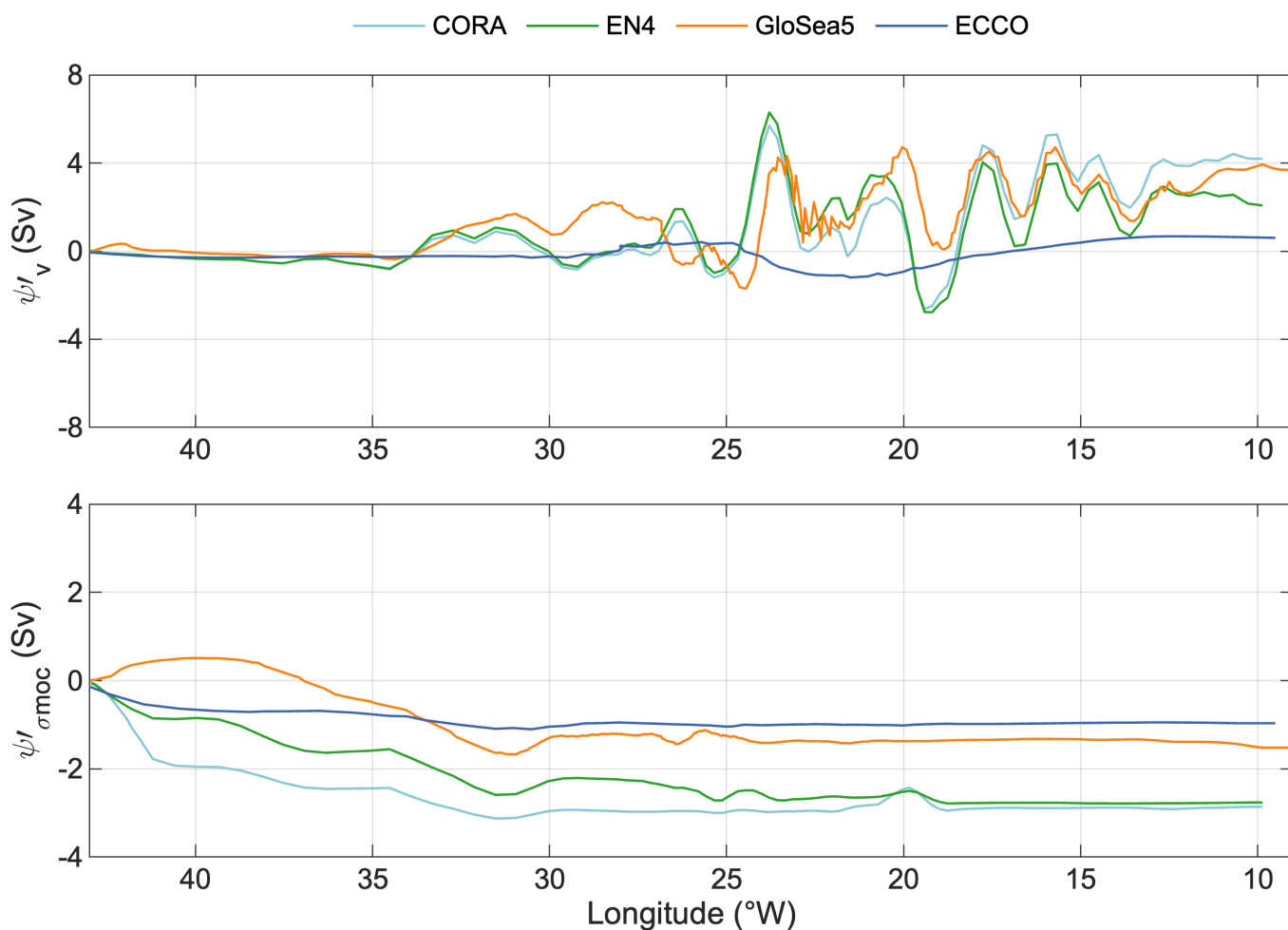
465

Figure 10: Transport difference (Sv) between 2015-2018 and 2004-2008 accumulated in the MOC upper limb from the western boundary eastward along the OVIDE line for ψ'_v (upper panel) and $\psi'_{\sigma_{moc}}$ (lower panel). CORA is reported in light blue, EN4 in green, GloSea5 in orange and ECCO in blue.

5 Discussion

470 The mean value of the MOC at OVIDE is between 19.7 Sv and 20.3 Sv for EN4, CORA and GloSea5 while it is 15.3 Sv for ECCO. Estimates based on OVIDE hydrographic sections suggest that the MOC is underestimated by ECCO. At the same time, ECCO is the only estimator to use a four-dimensional variational estimation method ensuring dynamic consistency over the entire estimation period (1992–2017). Across OVIDE, the NAC transport appears decisive in determining the mean MOC strength. At 60°N, the mean value of upper limb MOC transport at OSNAP-East (Figure 1) was estimated at 17.9 ± 0.6 Sv for

2014-2020 (Fu et al. 2023). Note that this value was obtained by adding 1.6 Sv to the MOC lower limb transport of 16.3 Sv given by Fu et al. (2023) in order to account for a net northward transport of 1.6 Sv through OSNAP-East. The net northward transport must be added to OSNAP MOC lower limb transport as it is included in MOC strengths determined by integrating the meridional overturning stream functions from the surface, as we do here. During 2014–2020, the time-mean transport of the MOC upper limb at OVIDE (average between CORA, EN4, Glosea5) has a strength of 20.2 ± 0.3 Sv showing a difference of 2.3 Sv with OSNAP-East observations. This is also what is suggested by the analysis of GloSea5, which shows that the MOC at OSNAP-East is 1.2 (1.4) Sv lower than the MOC at OVIDE for the period 2014-2020 (1993-2021). The difference between the MOC at OVIDE and the MOC at OSNAP-East is most likely explained by water mass transformations in the Iceland Basin and Rockall Trough between the two sections (Desbruyères et al., 2019). Desbruyères et al. (2019) estimated a difference of 4.2 Sv between the surface-forced transformation rates North of 45°N and North of OSNAP-East whose order of magnitude positively echoes our results. Interestingly, the MOC at OVIDE and the MOC at OSNAP-East estimated from GloSea5 show that the two series are significantly correlated (0.83, p < 0.001) (Figure S3) suggesting that the same mechanisms drive the variability of the MOC at the two lines for the most energetic seasonal and decadal time scales.
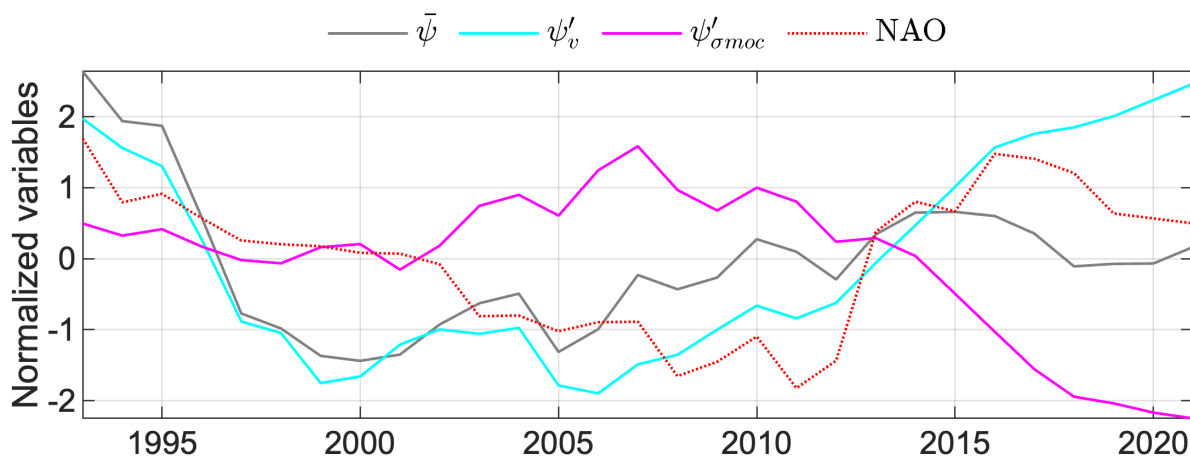
Figure 11: Winter NAO (dotted red line), ψ' (grey), ψ'_v (cyan) and $\psi'_{\sigma moc}$ (magenta). ψ', ψ'_v and $\psi'_{\sigma moc}$ are the average of CORA, EN4 and GloSea5. Time series were normalized by their standard deviations and low-pass filtered using a moving mean with a 60-month window.

Seasonal density changes in the upper EGC drive the seasonal cycle of the MOC. Using OSNAP data over the period 2014–2016, Le Bras et al. (2020) linked density changes in the EGC to the intermittent presence of Irminger Sea Intermediate Water (ISIW, 32.23 to 32.38 kg m^{-3} in σ_1), a water mass formed offshore of the EGC and which joins this western boundary current by eddy-driven subduction. We observed that the seasonal change in density in the EGC generates a seasonal adjustment of σ_{moc} that leads to a change in the volume of the upper limb of the MOC in the EGC and an opposite volume change in the NAC. These volume changes result in perturbations of the MOC strength, which combine to increase the MOC strength in winter and decrease it in summer and autumn. The numerical study by Tooth et al (2023) reached the same conclusion about the importance of changes in the MOC branch volumes in explaining seasonality at OSNAP-East and identifies seasonal changes in EGC transport as a key component of seasonality. Along OVIDE, the velocity-driven seasonality is dominated by the eastern boundary current transport which opposes the volume-driven changes in late autumn. Analyzing the seasonality at OSNAP-East, Fu et al. (2023) observed a maximum MOC strength in May and a minimum in December with a peak-to-trough amplitude of 6.2 Sv similar to the amplitudes of the CORA and EN4 seasonal cycle, which are in the high range of our estimates. The Ekman transport contributes significantly to the seasonal cycle at OSNAP-East with a peak-to-trough amplitude of 2.4 Sv between May and December, higher than the amplitude of 1.7 Sv observed between June and November at OVIDE. The difference in amplitude of the Ekman transport between OSNAP-East and OVIDE is due to differences in the orientation of the sections (Figure 1). Fu

et al. (2023) linked the seasonal variability of the MOC at OSNAP-East to that of the water mass transformation to the north of the section and to the rapid export of upper North Atlantic Deep Water (NADW, 32.23 to 32.38 kg m^{-3} in σ_1) by the EGC, which causes a maximum of overturning 3-5 months after the occurrence of the transformation maximum (see also Li et al., 2019). The OVIDE and OSNAP-East lines follow the same path in the Irminger Sea and by linking the density variations in the EGC to volume anomalies in the MOC limbs and to MOC strength anomalies, our results shed additional light on the results of Fu et al. (2023). A noteworthy result is that the seasonal cycle is controlled by the transformations of the water mass surrounding the density of σ_{moc}.

On a decadal scale, Jackson et al. (2022) conclude that there is evidence that MOC in the subpolar gyre declined from the mid-1990s to 2010 and has intensified since then. Fu et al. (2020) argue that MOC has been stable in the subpolar gyre since 1980. Fraser et al (2021) show a stable MOC at 50°N between the mid-1990s and the mid-2000s, followed by a decrease until 2015. Regardless of the analysis considered, we do not observe in this study any significant trends in the time series over the entire period analyzed. However a majority of analyses show a decrease in the first part of the time series, followed by a rather low MOC in 2000-2008, followed by an increase until 2018, in agreement with the conclusions of Jackson et al. (2022).

The transformation of light water masses into dense water masses in the subpolar gyre and in particular the resulting density changes in the Irminger Sea are key to the decadal-scale variability of the subpolar overturning (Figures 9 and 10). On decadal timescales, density changes in the deep convection region of the Irminger Sea lead to velocity-driven MOC changes partly offset by volume-driven changes. Interestingly, velocity-driven MOC changes are associated here with changes in NAC transport, which have already been identified in previous studies as a key element in explaining AMOC variability (Desbruyères et al., 2013; Desbruyères et al., 2015; Kostov et al., 2023). Chafik et al. (2022) showed that the density (annual mean, vertically averaged over the first 1000 m) in the Irminger Sea was correlated with the amplitude of the annual mean MOC at OSNAP-East over 1993–2018. We speculate that the Irminger Sea density anomaly calculated by Chafik et al. (2022) is representative of the density anomaly observed in Figure 9, which drives both ψ'_v and $\psi'_{\sigma_{moc}}$. Roussenov et al. (2022) identified the variability of the density field in the Irminger Sea as an indicator of MOC variability at OSNAP-East by linking a positive (negative) density anomaly in the Irminger Sea to a positive (negative) MOC strength anomaly using the Mongomery potential. In agreement with these results, we have shown in section 4.4 that the density field in the Irminger Sea acts on ψ'_v, increasing (decreasing) the MOC strength when the density anomaly is positive (negative). Analyzing four years of OSNAP measurements (2014-2018), Li et al. (2019) did not find any relationship between density anomalies in the EGC and subpolar overturning. Here we show that density variations in the Irminger Sea influence the volume of the MOC on decadal time scales and hence the MOC itself via $\psi'_{\sigma_{moc}}$ (Figure 10). However on a decadal time scale, $\psi'_{\sigma_{moc}}$ and ψ'_v are in opposition. In particular, during the period 2014-2018, which saw exceptional deep convection in the Irminger Sea (Piron et al., 2017), the overturning stream function anomalies $\psi'_{\sigma_{moc}}$ and ψ'_v have the same order of magnitude but are of opposite sign (Figure 10). This ultimately results in small MOC anomalies, and cancels the correlation between density anomalies in the Irminger Sea and MOC variability, showing the difficulty of understanding the variability of the MOC using an approach based solely on the analysis of density anomalies.

The North Atlantic Oscillation (NAO see Hurrell, 1995) is known to be the driver of density field changes in deep convection zones in the Labrador and Irminger Seas (Yashyaev et al., 2016; Piron et al., 2017; de Jong and de Steur, 2016). However, there is no one-to-one relationship. For example, Zunino et al. (2020) showed that the preconditioning of the water column by advection from the Labrador Sea allowed deep convection to continue southeast of Cape Farewell (Greenland) over the period 2014–2018 after the exceptional NAO winter of 2014 and despite forcing conditions returning to the average conditions. Russonov et al (2022) circumvented this difficulty by constructing composites from strong NAO events (greater than 1.6 times

the standard deviation) and showed that strong NAO events were associated with positive Irminger Sea density field anomalies and positive MOC anomalies. The MOC decomposition time series averaged of CORA, EN4 and GloSea5 (Figure 11) suggest that ψ'_v is correlated (r=0.74, p=0.15) on decadal scales with the NAO and that $\psi'_{\sigma_{moc}}$ is anti-correlated (r=-0.61, p=0.21) (ECCO was not included in the average because it differs very significantly from the other estimates). The MOC strength ψ' is positively correlated with NAO (r=0.50; p=0.38), which is consistent with the fact that, on longer time scales, the variability of the MOC strength is mainly driven by ψ'_v. Numerous modeling studies suggest that on decadal scales the NAO precedes MOC variability (see Kim et al., 2023 for a review) but our time series are too short to confirm this statistically. In the end, the anti-correlation between ψ'_v and $\psi'_{\sigma_{moc}}$ suggests that the decomposition used in this paper applied to historical climate model runs could provide more insight into the variability of MOC and atmospheric forcing.

In addition to the way in which the analyses take the observations into account (objective analysis, 3D-var assimilation, 4D-var assimilation), several factors contributing to the differences in MOC observed between the analyses can be mentioned. EN4 and CORA use the same data sets and an objective analysis but differ in their choice of spatial correlation functions and therefore in the spatial scales selected. Dynamics play a more significant role in the interpolation of data by GloSea5 and ECCO, but given the different spatial resolutions of the ocean models (0.25° and 1° respectively) the way in which eddies are taken into account differs. The reconstruction of the seasonal variability of the MOC, for which the density field west of the Irminger Sea is a key parameter, is also challenged by the limitations of the data sets. While high-precision altimetry began in 1993, the Argo network was not deployed until 2002. Argo floats have little or no coverage of water depths below 1000 m and satellite altimetry will be limited for periods when the Greenland shelf is covered by sea ice. Despite these limitations, our results have highlighted the respective roles of $of\ \psi'_v\ and\ \psi'_{\sigma moc}$ in the variability of the subpolar MOC.

6 Concluding remarks

We studied the evolution of the MOC between Greenland and Portugal over almost three decades using four different data-driven estimators. The MOC measurements ψ_{hydro} taken during the OVIDE cruises showed good agreement with the analyses where the weight of the data was the highest ($\psi_{cora}, \psi_{en4}, \psi_{glosea5}$). The state estimates ψ_{ecco} deviates more from our direct observations. OVIDE biennial observations have therefore been decisive in enabling a critical assessment of the data-driven estimators.

Although they are essentially based on the same data sets, the four analyses do show some differences, for example in the seasonal cycle of the MOC, the amplitude of which varies by a factor of two between the analyses, or the difference between ECCO and the other analyses in the reproduction of the decadal variability of the MOC for the 1990s. However, the decomposition into velocity-driven and volume-driven components made it possible to identify variability mechanisms common to all the analyses. Thus, the seasonal variability can be ascribed to volume variations in the EGC and to transport variations at the eastern boundary. Decadal variation in MOC is driven by velocity in the 1990s. While dominated by the velocity component, decadal variation in MOC strength in the years 2005 to 2021 is damped by the volume component.

Data availability

OVIDE Hydrographic data are available from https://www.seanoe.org/data/00353/46448/ (Mercier et al., 2022). CORA v5.2 objectively mapped fields are available on https://data.marine.copernicus.eu/product/INSITU_GLO_PHY_TS_OA_MY_013_052/services; EN4 objective analyses on

https://www.metoffice.gov.uk/hadobs/en4/download-en4-2-2.html; GloSea5 reanalysis on
590 https://data.marine.copernicus.eu/product/GLOBAL_REANALYSIS_PHY_001_031/description; ECCO fields on
https://podaac.jpl.nasa.gov/ECCO?tab=mission-objectives§ions=about%2Bdata; NCEP/NCAR atmospheric analysis on
https://psl.noaa.gov/data/gridded/data.ncep.reanalysis.html; AVISO altimeter on http://marine.copernicus.eu/services-
portfolio/access-to-products/; NAO index on
https://www.cpc.ncep.noaa.gov/products/precip/CWlink/pna/norm.nao.monthly.b5001.current.ascii.table. MOC time series
595 across OVIDE are available from the Supplement.

Authors' contributions

HM and DD conceived the study. HM made the computation and wrote the first draft (PL provided the inverse model results for 2016–2021). All authors discussed the results and reviewed two successive drafts.

Competing interests

600 The authors declare that they have no conflict of interest.

Acknowledgements

This work received funding from the European Union's Horizon 2020 research and innovation programme under grant agreement No 862626 (EUROSEA), the French National Programme Les Enveloppes Fluides et l'Environnement (LEFE) and Ifremer. HM was supported by the Centre National de La Recherche Scientifique (CNRS). FF and AV were supported by the BOCATS2
605 (PID2019-104279GB-C21) project funded by MCIN/AEI/10.13039/501100011033 and together with LH, by EuroGO-SHIP project (Horizon Europe #101094690). MF was supported by grant PTA2022-021307-I funded by MCIN/AEI/10.13039/501100011033, by European Social Fund Plus, and by the Portuguese Foundation for Science and Technology through projects UIDB/04326/2020 (doi:10.54499/UIDB/04326/2020), UIDP/04326/2020 (doi:10.54499/UIDP/04326/2020), LA/P/0101/2020 (doi:10.54499/LA/P/0101/2020) and CEECINST/00114/2018. We
610 gratefully acknowledge support from the French Oceanographic Fleet to OVIDE (https://doi.org/10.18142/140). We thank L. Jackson for providing GloSea5 data on the native grid. Colormaps are from MatPlotLib Perceptually Uniform Colormaps.

References

Le Bras, I. A., Straneo, F., Holte, J., De Jong, M. F., and Holliday, N. P.: Rapid Export of Waters Formed by Convection Near the Irminger Sea's Western Boundary, Geophys. Res. Lett., 47, https://doi.org/10.1029/2019GL085989, 2020.

615 Böning, C. W., Scheinert, M., Dengg, J., Biastoch, a., and Funk, a.: Decadal variability of subpolar gyre transport and its reverberation in the North Atlantic overturning, Geophys. Res. Lett., 33, 1–5, https://doi.org/10.1029/2006GL026906, 2006.

Bretherton, C. S., Widmann, M., Dymnikov, valentin P., Wallace, J. M., and Bladé, I.: The Effective Number of Spatial Degrees of Freedom of a Time-Varying Field, J. Clim., 12, 1990–2009, 1999.

620 Bryden, H. L., Johns, W. E., King, B. A., McCarthy, G. D., McDonagh, E. L., Moat, B. I., and Smeed, D. A.: Reduction in Ocean Heat Transport at 26°N since 2008 Cools the Eastern Subpolar Gyre of the North Atlantic Ocean, J. Clim., 33, 1677–1689, https://doi.org/10.1175/JCLI-D-19-0323.1, 2020.

Chafik, L., Holliday, N. P., Bacon, S., and Rossby, T.: Irminger Sea Is the Center of Action for Subpolar AMOC Variability Geophysical Research Letters, Geophys. Res. Lett., 49, https://doi.org/10.1029/2022GL099133, 2022.

625   Cheng, L. and Zhu, J.: Artifacts in variations of ocean heat content induced by the observation system changes, Geophys. Res. Lett., 7276–7283, https://doi.org/10.1002/2014GL061881.Received, 2014.

Cumming, G., Fidler, F., and Vaux, D. L.: Error bars in experimental biology, J. Cell Biol., 177, 7–11, https://doi.org/10.1083/jcb.200611141, 2007.

Daniault, N., Mercier, H., Lherminier, P., Sarafanov, A., Falina, A., Zunino, P., Pérez, F. F., Ríos, A. F., Ferron, B., Huck, T.,
630   and Thierry, V.: The northern North Atlantic Ocean mean circulation in the early 21st century, Prog. Oceanogr., 146, 142–158, https://doi.org/10.1016/j.pocean.2016.06.007, 2016.

Desbruyères, D., Thierry, V., and Mercier, H.: Simulated decadal variability of the meridional overturning circulation across the A25-Ovide section, J. Geophys. Res. Ocean., 118, https://doi.org/10.1029/2012JC008342, 2013a.

Desbruyères, D.: The meridional overturning circulation variability and heat content changes in the north atlantic subpolar the
635   Meridional Overturning Circulation Variability and Heat Content Canges in the North Atlantic Subpolar Gyre. Ph.D. thesis, Université de Bretagne Occidentale, 2013b.

Desbruyères, D., Mercier, H., and Thierry, V.: On the mechanisms behind decadal heat content changes in the eastern subpolar gyre, Prog. Oceanogr., 132, 262–272, https://doi.org/10.1016/j.pocean.2014.02.005, 2015.

Desbruyères, D. G., Mercier, H., Maze, G., and Daniault, N.: Surface predictor of overturning circulation and heat content change
640   in the subpolar North Atlantic, Ocean Sci., 15, https://doi.org/10.5194/os-15-809-2019, 2019.

Desbruyères, D., Chafik, L., and Maze, G.: A shift in the ocean circulation has warmed the subpolar North Atlantic Ocean since 2016, Commun. earth Environ., https://doi.org/10.1038/s43247-021-00120-y, 2021.

Frajka-Williams, E., Ansorge, I. J., Baehr, J., Bryden, H. L., Chidichimo, M. P., Cunningham, S. A., Danabasoglu, G., Dong, S., Donohue, K. A., Elipot, S., Heimbach, P., Holliday, N. P., Hummels, R., Jackson, L. C., Karstensen, J., Lankhorst, M., Le
645   Bras, I. A., Susan Lozier, M., McDonagh, E. L., Meinen, C. S., Mercier, H., Moat, B. I., Perez, R. C., Piecuch, C. G., Rhein, M., Srokosz, M. A., Trenberth, K. E., Bacon, S., Forget, G., Goni, G., Kieke, D., Koelling, J., Lamont, T., McCarthy, G. D., Mertens, C., Send, U., Smeed, D. A., Speich, S., van den Berg, M., Volkov, D., and Wilson, C.: Atlantic meridional overturning circulation: Observed transport and variability, Front. Mar. Sci., 6, https://doi.org/10.3389/fmars.2019.00260, 2019.

650   Fu, Y., Lozier, M. S., Biló, T. C., Bower, A. S., Cunningham, S. A., Cyr, F., Jong, M. F. De, Drysdale, L., Fraser, N., Fried, N., Furey, H. H., Han, G., Handmann, P., Holliday, N. P., Holte, J., Inall, M. E., Johns, W. E., Jones, S., Karstensen, J., Li, F., Pacini, A., Pickart, R. S., Rayner, D., Straneo, F., and Yashayaev, I.: Seasonality of the Meridional Overturning Circulation in the subpolar North Atlantic, Commun. earth Environ., 4:181, https://doi.org/10.1038/s43247-023-00848-9, 2023.

Fukumori, I., Heimbach, P., Ponte, R. M., and Wunsch, C.: A dynamically consistent, multivariable ocean climatology, Bull.
655   Am. Meteorol. Soc., 2107–2128, https://doi.org/10.1175/BAMS-D-17-0213.1, 2018.

Good, S. A., Martin, M. J., and Rayner, N. A.: EN4 : Quality controlled ocean temperature and salinity profiles and monthly objective analyses with uncertainty estimates, J. Geophys. Res. Ocean., 118, 6704–6716, https://doi.org/10.1002/2013JC009067, 2013.

Gourcuff, C., Lherminier, P., Mercier, H., and Le Traon, P. Y.: Altimetry combined with hydrography for ocean transport
660   estimation, J. Atmos. Ocean. Technol., 28, https://doi.org/10.1175/2011JTECHO818.1, 2011.

Hurrell, J. W.: Decadal trends in the North Atlantic oscillation: regional temperatures and precipitation. Science, 269, 676–679, doi: 10.1126/science.269.5224.676, 1995.

Jackson, L. C., Peterson, K. A., Roberts, C. D., and Wood, R. A.: Recent slowing of Atlantic overturning circulation as a recovery from earlier strengthening, Nat. Geosci., 9, 518–522, https://doi.org/10.1038/NGEO2715, 2016.

665   Jackson, L. C., Dubois, C., Forget, et al. (19 authors): The Mean State and Variability of the North Atlantic Circulation : A Perspective From Ocean Reanalyses Journal of Geophysical Research : Oceans, J. Geophys. Res. Ocean., 124, 9141–9170, https://doi.org/10.1029/2019JC015210, 2019.

Jackson, L. C., Biastoch, A., Buckley, M. W., Desbruyères, D. G., Williams, E. F., Moat, B., and Robson, J.: The evolution of the North Atlantic meridional overturning circulation since 1980, Nat. Rev. Earth Environ., https://doi.org/10.1038/s43017-022-00263-2, 2022.

de Jong, M. F., and de Steur, L.: Strong winter cooling over the Irminger Sea in winter 2014–2015, exceptional deep convection, and the emergence of anomalously low SST, Geophys. Res. Lett., 43, 7106–7113, 2016. https://doi.org/10.1002/2016GL069596.

de Jong, M. F., Oltmanns, M., Karstensen, J., and de Steur, L.: Deep convection in the Irminger Sea observed with a dense mooring array., Oceanography, 31, 50–59, 2018.

Johns, W. E., Elipot, S., Smeed, D. A., Moat, B., King, B., Volkov, D. L., and Smith, R. H.: Towards two decades of Atlantic Ocean mass and heat transports at 26.5° N, Philos. Trans. A. Math. Phys. Eng. Sci., 381, 20220188, https://doi.org/10.1098/rsta.2022.0188, 2023.

Jousset S., Mulet S., Wilkin J., Greiner E., Dibarboure G. and Picot N.: "New global Mean Dynamic Topography CNES-CLS-22 combining drifters, hydrological profiles and High Frequency radar data", OSTST 2022, https://doi.org/10.24400/527896/a03-2022.3292.

Kalnay, E., Kanamitsu, M., Kistler, R., Collins, W., Deaven, D., and Gandin, L.: The NCEP / NCAR 40-Year Reanalysis Project, Bull. Am. Meteorol. Soc., 77, 437–471, 1996.

Kanzow, T., Cunningham, S. A., Johns, W. E., Hirschi, J. J.-M., Marotzke, J., Baringer, M. O., Meinen, C. S., Chidichimo, M. P., Atkinson, C., Beal, L. M., Bryden, H. L., and Collins, J.: Seasonal Variability of the Atlantic Meridional Overturning Circulation at 26.5° N, J. Clim., 23, 5678–5698, https://doi.org/10.1175/2010JCLI3389.1, 2010.

Kim, H., Park, J., Kim, D., and Kim, J.: North Atlantic Oscillation impact on the Atlantic Meridional Overturning Circulation shaped by the mean state, npj Clim. Atmos. Sci., 6, https://doi.org/10.1038/s41612-023-00354-x, 2023.

Kostov, Y., Johnson, H. L., Marshall, D. P., Heimbach, P., Forget, G., Holliday, N. P., Lozier, M. S., Li, F., Pillar, H. R., and Smith, T.: Distinct sources of interannual subtropical and subpolar Atlantic overturning variability, Nat. Geosci., 14, 491–495, https://doi.org/10.1038/S41561-021-00759-4, 2021.

Kostov, Y., Messias, M. J., Mercier, H., Johnson, H. L., and Marshall, D. P.: Fast mechanisms linking the Labrador Sea with subtropical Atlantic overturning, Clim. Dyn., 60, 2687–2712, https://doi.org/10.1007/s00382-022-06459-y, 2023.

Lherminier, P., Mercier, H., Gourcuff, C., Alvarez, M., Bacon, S., and Kermabon, C.: Transports across the 2002 Greenland-Portugal Ovide section and comparison with 1997, J. Geophys. Res., 112, C07003, https://doi.org/10.1029/2006JC003716, 2007.

Lherminier, P., Mercier, H., Huck, T., Gourcuff, C., Perez, F. F., Morin, P., Sarafanov, A., and Falina, A.: The Atlantic Meridional Overturning Circulation and the subpolar gyre observed at the A25-OVIDE section in June 2002 and 2004, Deep. Res. Part I Oceanogr. Res. Pap., 57, 1374–1391, https://doi.org/10.1016/j.dsr.2010.07.009, 2010.

Li, F., Lozier, M. S., Bacon, S., Bower, A. S., Cunningham, S. A., De Jong, M. F., Fraser, N., Fried, N., Han, G., Holliday, N. P., Holte, J., Houpert, L., Inall, M. E., Johns, W. E., Jones, S., Johnson, C., Karstensen, J., Le Bras, I. A., Lherminier, P., Lin, X., Mercier, H., Oltmanns, M., Pacini, A., Petit, T., Pickart, R. S., Rayner, D., Straneo, F., Thierry, V., Visbeck, M., Yashayaev, I., and Zhou, C.: Subpolar North Atlantic western boundary density anomalies and the Meridional Overturning Circulation, 12:3002, 1–9, https://doi.org/10.1038/s41467-021-23350-2, 2021.

Lozier, S. M., Li, F., Bacon, S., and et al.: A sea change in our view of overturning in the subpolar North Atlantic, Science (80-.)., 363, 516–521, 2019.

Lynch-stieglitz, J.: The Atlantic Meridional Overturning Circulation and Abrupt Climate Change, Annu. Rev. Mar. Sci., 9, 83:104, https://doi.org/10.1146/annurev-marine-010816-060415, 2017.

Maclachlan, C., Arribas, A., Peterson, K. A., Maidens, A., Fereday, D., Scaife, A. A., Gordon, M., Vellinga, M., Williams, A.,
710 Comer, R. E., Camp, J., Xavier, P., Madec, G., and National, F.: Global Seasonal forecast system version 5 (GloSea5): a
high-resolution seasonal forecast system, 5, 1072–1084, https://doi.org/10.1002/qj.2396, 2015.

McCarthy, G., Frajka-Williams, E., Johns, W. E., Baringer, M. O., Meinen, C. S., Bryden, H. L., Rayner, D., Duchez, A., Roberts,
C., and Cunningham, S. A.: Observed interannual variability of the Atlantic meridional overturning circulation at 26.5°N,
Geophys. Res. Lett., 39, n/a-n/a, https://doi.org/10.1029/2012GL052933, 2012.

715 McCarthy, G. D., Brown, P. J., Flagg, C. N., and et al.: Sustainable Observations of the AMOC : Methodology and Technology,
Rev. Geophys., 58, 1–34, https://doi.org/10.1029/2019RG000654, 2020.

Mercier, H., Lherminier, P., Sarafanov, A., Gaillard, F., Daniault, N., Desbruyères, D., Falina, A., Ferron, B., Gourcuff, C.,
Huck, T., and Thierry, V.: Variability of the meridional overturning circulation at the Greenland–Portugal OVIDE section
from 1993 to 2010, Prog. Oceanogr., 132, 250–261, https://doi.org/10.1016/j.pocean.2013.11.001, 2015.

720 Mercier, H., Lherminier, P., and Pérez, Fiz F.: The Greenland-Portugal Go-Ship A25 OVIDE CTDO$_2$ hydrographic data.
SEANOE. https://doi.org/10.17882/46448, 2022.

Messias, M. J. and Mercier, H.: The redistribution of anthropogenic excess heat is a key driver of warming in the North Atlantic,
Commun. Earth Environ., 3, https://doi.org/10.1038/s43247-022-00443-4, 2022.

Moat, B. I., Smeed, D. A., Frajka-Williams, E., Desbruyères, D. G., Beaulieu, C., Johns, W. E., Rayner, D., Sanchez-Franks, A.,
725 Baringer, M. O., Volkov, D., Jackson, L. C., and Bryden, H. L.: Pending recovery in the strength of the meridional
overturning circulation at 26° N, Ocean Sci., 16, 863–874, https://doi.org/10.5194/os-16-863-2020, 2020.

Mudelsee, M.: Trend analysis of climate time series : A review of methods, Earth-Science Rev., 190, 310–322,
https://doi.org/10.1016/j.earscirev.2018.12.005, 2019.

Nguyen, A. T., Pillar, H., Ocaña, V., Bigdeli, A., Smith, T. A., and Heimbach, P.: The Arctic Subpolar Gyre sTate Estimate :
730 Description and Assessment of a Data-Constrained , Dynamically Consistent Ocean-Sea Ice Estimate for 2002 – 2017, J.
Adv. Model. Earth Syst., e2020MS002, https://doi.org/10.1029/2020MS002398, 2020.

Pérez, F. F., Mercier, H., Vázquez-Rodríguez, M., Lherminier, P., Velo, A., Pardo, P. C., Rosón, G., and Ríos, A. F.: Atlantic
Ocean CO$_2$ uptake reduced by weakening of the meridional overturning circulation, Nat. Geosci., 6,
https://doi.org/10.1038/ngeo1680, 2013.

735 Petit, T., Lozier, M. S., Josey, S. A., and Cunningham, S. A.: Atlantic Deep Water Formation Occurs Primarily in the Iceland
Basin and Irminger Sea by Local Buoyancy Forcing, Geophys. Res. Lett., 47, https://doi.org/10.1029/2020GL091028,
2020.

Piron, A., Thierry, V., Mercier, H., and Caniaux, G.: Argo float observations of basin-scale deep convection in the Irminger sea
during winter 2011–2012, Deep. Res. Part I Oceanogr. Res. Pap., 109, https://doi.org/10.1016/j.dsr.2015.12.012, 2016.

740 Piron, A., Thierry, V., Mercier, H., and Caniaux, G.: Gyre-scale deep convection in the subpolar North Atlantic Ocean during
winter 2014-2015, Geophys. Res. Lett., 44, https://doi.org/10.1002/2016GL071895, 2017.

Robson, J., Hodson, D., Hawkins, E., and Sutton, R.: Atlantic overturning in decline?, Nat. Geosci., 7, 2–3,
https://doi.org/10.1038/ngeo2050, 2014.

Roussenov, V. M., Williams, R. G., Lozier, M. S., Holliday, N. P., and Smith, D. M.: Historical Reconstruction of Subpolar
745 North Atlantic Overturning and Its Relationship to Density, J. Geophys. Res. Ocean., 127, 1–24,
https://doi.org/10.1029/2021JC017732, 2022.

Scaife, A. A., Arribas, A., Blockey, E., Brookshaw, A., Clark, R. T., Dunstone, N., Eade, R., Fereday, D., Folland, C. K., Gordon,
M., Hermanson, L., Kniwght, J. R., Lea, D. J., MacLachlan, C., Maidens, A., Martin, M., Peterson, A. K., Smith, D.,
Vellinga, M., Wallace, E., Waters, J., and Williams, A.: Geophysical Research Letters, Geophys. Res. Lett., 41, 2514–
750 2519, https://doi.org/doi:10.1002/2014GL059637, 2014.

Smeed, D. A., Josey, S. A., Beaulieu, C., Johns, W. E., Moat, B. I., Frajka-Williams, E., Rayner, D., Meinen, C. S., Baringer, M. O., Bryden, H. L., and McCarthy, G. D.: The North Atlantic Ocean Is in a State of Reduced Overturning, Geophys. Res. Lett., 45, 1527–1533, https://doi.org/10.1002/2017GL076350, 2018.

Srokosz, M. a. and Bryden, H. L.: Observing the Atlantic Meridional Overturning Circulation yields a decade of inevitable surprises, Science (80-.)., 348, 1255575–1255575, https://doi.org/10.1126/science.1255575, 2015.

Szekely, T., Gourrion, J., Pouliquen, S., Reverdin, G., Ird, C., and Locean, M.: The CORA 5 . 2 dataset for global in situ temperature and salinity measurements : data description and validation, Ocean Sci., 15, 1601–1614, 2019.

Thomson, R. E. and Emery, W. J.: Data Analysis Methods in Physical Oceanography: Third Edition, Elsevier Science, 712 pp., https://doi.org/10.1016/C2010-0-66362-0, 2014.

Wang, H., Zhao, J., Li, F., and Lin, X.: Seasonal and Interannual Variability of the Meridional Overturning Circulation in the Subpolar North Atlantic Diagnosed From a High Resolution Reanalysis Data Set, J. Geophys. Res. Ocean., 126, 1–19, https://doi.org/10.1029/2020JC017130, 2021.

Weijer, W., Cheng, W., Garuba, O. A., Hu, A., and Nadiga, B. T.: CMIP6 Models Predict Significant 21st Century Decline of the Atlantic Meridional Overturning Circulation, Geophys. Res. Lett., 47, https://doi.org/10.1029/2019GL086075, 2020.

Williams, R. G., Katavouta, A., and Roussenov, V.: Regional asymmetries in ocean heat and carbon storage due to dynamic redistribution in climate model projections, J. Clim., 34, 3907–3925, https://doi.org/10.1175/JCLI-D-20-0519.1, 2021.

Worthington, E. L., Moat, B. I., Smeed, D. A., Mecking, J. V, Marsh, R., and Mccarthy, G. D.: A 30-year reconstruction of the Atlantic meridional overturning circulation shows no decline, Ocean Sci., 17, 285–299, 2021. https://doi.org/10.5194/os-17-285-2021

Yashayaev, I. and Loder, J. W.: Recurrent replenishment of Labrador Sea Water and associated decadal-scale variability, J. Geophys. Res. Ocean., 8095–8114, https://doi.org/10.1002/2016JC012046.Received, 2016.

Yeager, S., Castruccio, F., Chang, P., Danabasoglu, G., Maroon, E., Small, J., Wang, H., Wu, L., and Zhang, S.: An outsized role for the Labrador Sea in the multidecadal variability of the Atlantic overturning circulation, Sci. Adv., 7, https://doi.org/10.1126/sciadv.abh3592, 2021.

Zhang, R.: Latitudinal dependence of Atlantic meridional overturning circulation (AMOC) variations, Geophys. Res. Lett., 37, 1–6, https://doi.org/10.1029/2010GL044474, 2010.

Zhao, J. and Johns, W.: Wind-Driven Seasonal Cycle of the Atlantic Meridional Overturning Circulation, J. Phys. Oceanogr., 44, 1541–1562, https://doi.org/10.1175/JPO-D-13-0144.1, 2014a.

Zhao, J. and Johns, W.: Wind-forced interannual variability of the Atlantic Meridional Overturning Circulation at 26.5 N, J. Geophys. Res. Ocean., 2403–2419, https://doi.org/10.1002/2013JC009407.Received, 2014b.

Zou, S., Lozier, S. M., and Buckley, M. W.: How Is Meridional Coherence Maintained in the Lower Limb of the Atlantic Meridional Overturning Circulation ? Geophysical Research Letters, Geophys. Res. Lett., 45, 1–9, https://doi.org/10.1029/2018GL080958, 2018.

Zunino, P., Lherminier, P., Mercier, H., Daniault, N., García-Ibáñez, M. I., and Pérez, F. F.: The GEOVIDE cruise in May-June 2014 reveals an intense Meridional Overturning Circulation over a cold and fresh subpolar North Atlantic, Biogeosciences, 14, https://doi.org/10.5194/bg-14-5323-2017, 2017.

Zunino, P., Mercier, H., and Thierry, V.: Why did deep convection persist over four consecutive winters (2015-2018) southeast of Cape Farewell?, Ocean Sci., 16, https://doi.org/10.5194/os-16-99-2020, 2020.

790